



NAVAL POSTGRADUATE SCHOOL

MONTEREY, CALIFORNIA

THESIS

**MODELING OF IMPRESSION TESTING TO OBTAIN
MECHANICAL PROPERTIES OF LEAD-FREE SOLDERS
MICROELECTRONIC INTERCONNECTS**

by

How, Yew Seng

December 2005

Thesis Advisor:

Indranath Dutta

Approved for public release; distribution is unlimited

THIS PAGE INTENTIONALLY LEFT BLANK

REPORT DOCUMENTATION PAGE			<i>Form Approved OMB No. 0704-0188</i>	
Public reporting burden for this collection of information is estimated to average 1 hour per response, including the time for reviewing instruction, searching existing data sources, gathering and maintaining the data needed, and completing and reviewing the collection of information. Send comments regarding this burden estimate or any other aspect of this collection of information, including suggestions for reducing this burden, to Washington headquarters Services, Directorate for Information Operations and Reports, 1215 Jefferson Davis Highway, Suite 1204, Arlington, VA 22202-4302, and to the Office of Management and Budget, Paperwork Reduction Project (0704-0188) Washington DC 20503.				
1. AGENCY USE ONLY (Leave blank)		2. REPORT DATE December 2005	3. REPORT TYPE AND DATES COVERED Master's Thesis	
4. TITLE AND SUBTITLE: Modeling of Impression Testing to Obtain Mechanical Properties of Lead-Free Solders Microelectronic Interconnects			5. FUNDING NUMBERS	
6. AUTHOR(S) Yew Seng How				
7. PERFORMING ORGANIZATION NAME(S) AND ADDRESS(ES) Naval Postgraduate School Monterey, CA 93943-5000			8. PERFORMING ORGANIZATION REPORT NUMBER	
9. SPONSORING /MONITORING AGENCY NAME(S) AND ADDRESS(ES) N/A			10. SPONSORING/MONITORING AGENCY REPORT NUMBER	
11. SUPPLEMENTARY NOTES The views expressed in this thesis are those of the author and do not reflect the official policy or position of the Department of Defense or the U.S. Government.				
12a. DISTRIBUTION / AVAILABILITY STATEMENT Approved for public release; distribution is unlimited			12b. DISTRIBUTION CODE	
13. ABSTRACT (maximum 200 words) <p>The increasing structural functionalities of materials in microelectronics and MEMs packages has led to an explosion of interest in characterizing the mechanical properties of small volumes of materials in the micrometer to nanometer regime. In microelectronics packages, one of the main challenges in reliability assessment is the prediction of solder joint failure during service applications. To a large extent, this is hindered by the difficulty in measuring the properties of micro-scale solder balls, which can be quite different from those of bulk solders.</p> <p>Recently, there has been substantial interest in miniaturized impression testing for measuring creep and other mechanical properties of microelectronic solder joints. Since impression testing produces punch stress versus impression strain data, it is necessary to find the appropriate correlations to convert the properties obtained by impression stress-strain testing to equivalent uniaxial properties.</p> <p>Therefore, in this work, finite element modeling using ANSYSTM is employed to obtain the elastic, plastic and creep properties of these Sn-Ag solder joints from impression testing, which uses a flat-tip cylindrical indenter, so that correlations may be drawn with corresponding properties from uniaxial testing.</p>				
14. SUBJECT TERMS Finite-element modeling, instrumented indentation, flat-tip indenter, lead-free solders, elastic and plastic properties, stress-strain plots			15. NUMBER OF PAGES 99	
			16. PRICE CODE	
17. SECURITY CLASSIFICATION OF REPORT Unclassified	18. SECURITY CLASSIFICATION OF THIS PAGE Unclassified	19. SECURITY CLASSIFICATION OF ABSTRACT Unclassified	20. LIMITATION OF ABSTRACT UL	

THIS PAGE INTENTIONALLY LEFT BLANK

Approved for public release; distribution is unlimited

**MODELING OF IMPRESSION TESTING TO OBTAIN MECHANICAL
PROPERTIES OF LEAD-FREE SOLDERS MICROELECTRONIC
INTERCONNECTS**

Yew Seng How
Singapore Technologies Engineering
B.Eng, National University of Singapore, 2002

Submitted in partial fulfillment of the
requirements for the degree of

**MASTER OF SCIENCE IN ENGINEERING SCIENCE
(MECHANICAL ENGINEERING)**

from the

**NAVAL POSTGRADUATE SCHOOL
December 2005**

Author: Yew Seng How

Approved by: Professor Indranath Dutta
Thesis Advisor

Distinguished Professor Anthony J. Healey
Chairman, Department of Mechanical and
Astronautical Engineering

THIS PAGE INTENTIONALLY LEFT BLANK

ABSTRACT

The increasing structural functionalities of materials in microelectronics and MEMs packages has led to an explosion of interest in characterizing the mechanical properties of small volumes of materials in the micrometer to nanometer regime. In microelectronics packages, one of the main challenges in reliability assessment is the prediction of solder joint failure during service applications. To a large extent, this is hindered by the difficulty in measuring the properties of micro-scale solder balls, which can be quite different from those of bulk solders.

Recently, there has been substantial interest in miniaturized impression testing for measuring creep and other mechanical properties of microelectronic solder joints. Since impression testing produces punch stress versus impression strain data, it is necessary to find the appropriate correlations to convert the properties obtained by impression stress-strain testing to equivalent uniaxial properties.

Therefore, in this work, finite element modeling using ANSYSTM is employed to obtain the elastic, plastic and creep properties of these Sn-Ag solder joints from impression testing, which uses a flat-tip cylindrical indenter, so that correlations may be drawn with corresponding properties from uniaxial testing.

THIS PAGE INTENTIONALLY LEFT BLANK

TABLE OF CONTENTS

I.	INTRODUCTION.....	1
A.	MEASUREMENT OF MECHANICAL PROPERTIES	1
1.	Overview.....	1
2.	Hardness Testing.....	1
B.	APPLICATIONS OF INDENTATION TECHNIQUES	2
1.	Micro-Electro-Mechanical Systems Challenges.....	2
2.	Thin Films.....	3
II.	LITERATURE REVIEW	5
A.	HISTORY OF IMPRESSION TESTING.....	5
B.	CURRENT INTEREST IN IMPRESSION TESTING.....	11
C.	OBJECTIVE AND SCOPE.....	22
1.	Elastic Properties	22
2.	Plastic Properties	23
3.	Creep Properties.....	24
III.	METHODOLOGY.....	25
A.	FINITE ELEMENT MODELING.....	25
1.	Overview.....	25
2.	Model Description.....	25
B.	MODEL INPUTS	28
1.	Material Properties	28
2.	Multi-linear Isotropic Stress-Strain Inputs.....	29
3.	Determination of Uniaxial Yield Strength	33
4.	Inputs for Investigation of Strain Rate Effects	36
5.	Multi-linear Stress Strain Inputs for Alternate Solder	36
IV.	RESULTS	41
A.	BILINEAR ISOTROPIC ANALYSIS FOR SN-AG SOLDER	41
1.	Impression Stress-Strain Plots for BISO Analysis	41
2.	Determination of Impression Elastic Modulus E^{BISO}_{imp} for BISO Analysis	43
3.	Determination of Impression Strain Hardening Coefficient K^{BISO}_{imp} for BISO Analysis	43
B.	MULTILINEAR ISOTROPIC ANALYSIS FOR SN-AG SOLDER.....	44
1.	Impression Stress-Strain Plots for MISO Analysis.....	44
2.	Determination of Impression Elastic Modulus E^{MISO}_{imp} for MISO Analysis.....	47
3.	Determination of Impression Yield Strength for MISO Analysis.....	47
4.	Determination of n_{imp} and K^{MISO}_{imp} Values for MISO Analysis.....	50

5.	Determination of m_{imp} and $n_{crp,imp}$ Values for MISO Analysis of Sn-Ag Solder	55
C.	MULTILINEAR ISOTROPIC ANALYSIS FOR ALTERNATE SOLDER	58
1.	Impression Stress-Strain Plots for MISO Analysis	58
2.	Determination of n_{imp} and K^{MISO}_{imp} Values for MISO Analysis	61
V.	DISCUSSION	65
A.	BILINEAR ISOTROPIC ANALYSIS FOR SN-AG SOLDER	65
1.	Correlation between E^{BISO}_{imp} and E	65
2.	Correlation between K^{BISO}_{imp} and K^{BISO}	66
B.	MULTILINEAR ISOTROPIC ANALYSIS FOR SN-AG SOLDER.....	67
1.	Correlation between E_{imp} and E	67
2.	Correlation between $\sigma_{YS,imp}$ and σ_{YS}	68
3.	Comparison of n_{imp} and n	69
4.	Correlation between K^{MISO}_{imp} and K^{MISO} for Sn-Ag Solder ..	70
5.	Comparison of m_{imp} and $n_{crp,imp}$ with m and n_{crp}	71
C.	MULTILINEAR ISOTROPIC ANALYSIS FOR ALTERNATE SOLDER	73
1.	Comparison of n_{imp} and n	73
2.	Correlation between K^{MISO}_{imp} and K^{MISO} for Alternate Solder	74
D.	RECOMMENDATION FOR FUTURE WORK	76
VI.	CONCLUSION	77
	LIST OF REFERENCES.....	79
	INITIAL DISTRIBUTION LIST	81

LIST OF FIGURES

Figure 1.	Finite Element Model of Impression Testing.....	27
Figure 2.	MISO Stress Strain Curve for Sn-Ag Solder – 298K.....	31
Figure 3.	MISO Stress Strain Curve for Sn-Ag – 323K.....	31
Figure 4.	MISO Stress Strain Curve for Sn-Ag Solder – 373K.....	32
Figure 5.	MISO Stress Strain Curve for Sn-Ag Solder – 423K.....	32
Figure 6.	MISO Input Uniaxial Yield Strength Determination – 298K.....	34
Figure 7.	MISO Input Uniaxial Yield Strength Determination – 323K.....	34
Figure 8.	MISO Input Uniaxial Yield Strength Determination – 373K.....	35
Figure 9.	MISO Input Uniaxial Yield Strength Determination – 423K.....	35
Figure 10.	MISO Stress Strain Curve for Alternate Solder – 298K	38
Figure 11.	MISO Stress Strain Curve for Alternate Solder – 323K	38
Figure 12.	MISO Stress Strain Curve for Alternate Solder – 373K	39
Figure 13.	MISO Stress Strain Curve for Alternate Solder – 423K	39
Figure 14.	BISO Impression Stress-Strain Plot for Sn-Ag Solder – 298K.....	41
Figure 15.	BISO Impression Stress-Strain Plot for Sn-Ag Solder – 323K.....	41
Figure 16.	BISO Impression Stress-Strain Plot for Sn-Ag Solder – 373K.....	42
Figure 17.	BISO Impression Stress-Strain Plot for Sn-Ag Solder – 423K.....	42
Figure 18.	MISO Impression Stress-Strain Plot for Sn-Ag Solder – 298K	45
Figure 19.	MISO Impression Stress-Strain Plot for Sn-Ag Solder – 323K	45
Figure 20.	MISO Impression Stress-Strain Plot for Sn-Ag Solder – 373K	46
Figure 21.	MISO Impression Stress-Strain Plot for Sn-Ag Solder – 423K	46
Figure 22.	MISO Impression Yield Strength Determination for Sn-Ag Solder at 298K.....	48
Figure 23.	MISO Impression Yield Strength Determination for Sn-Ag Solder at 323K	48
Figure 24.	MISO Impression Yield Strength Determination for Sn-Ag Solder at 373K	49
Figure 25.	MISO Impression Yield Strength Determination for Sn-Ag Solder at 423K.....	49
Figure 26.	Determination of $\sigma_{0,imp}$ at 298K.....	51
Figure 27.	Determination of $\sigma_{0,imp}$ at 323K.....	51
Figure 28.	Determination of $\sigma_{0,imp}$ at 373K.....	52
Figure 29.	Determination of $\sigma_{0,imp}$ at 423K.....	52
Figure 30.	Plot of $\ln (\sigma_{imp}-\sigma_{0,imp})$ vs $\ln \varepsilon_{pl,imp}$ for Sn-Ag Solder at 298K.....	53
Figure 31.	Plot of $\ln (\sigma_{imp}-\sigma_{0,imp})$ vs $\ln \varepsilon_{pl,imp}$ for Sn-Ag Solder at 323K.....	53
Figure 32.	Plot of $\ln (\sigma_{imp}-\sigma_{0,imp})$ vs $\ln \varepsilon_{pl,imp}$ for Sn-Ag Solder at 373K.....	54
Figure 33.	Plot of $\ln (\sigma_{imp}-\sigma_{0,imp})$ vs $\ln \varepsilon_{pl,imp}$ for Sn-Ag Solder at 423K.....	54
Figure 34.	Plot of $\ln \sigma_{imp}$ vs $\ln \dot{\varepsilon}_{pl,imp}$ for Sn-Ag Solder at 298K	56
Figure 35.	Plot of $\ln \sigma_{imp}$ vs $\ln \dot{\varepsilon}_{pl,imp}$ for Sn-Ag Solder at 323K	56
Figure 36.	Plot of $\ln \sigma_{imp}$ vs $\ln \dot{\varepsilon}_{pl,imp}$ for Sn-Ag Solder at 373K	57

Figure 37.	Plot of $\ln \sigma_{imp}$ vs $\ln \dot{\epsilon}_{pl,imp}$ for Sn-Ag Solder at 423K	57
Figure 38.	MISO Impression Stress-Strain Plot for Alternate Solder – 298K	59
Figure 39.	MISO Impression Stress-Strain Plot for Alternate Solder – 323K	59
Figure 40.	MISO Impression Stress-Strain Plot for Alternate Solder – 373K	60
Figure 41.	MISO Impression Stress-Strain Plot for Alternate Solder – 423K	60
Figure 42.	Plot of $\ln (\sigma_{imp} - \sigma_{0,imp})$ vs $\ln \epsilon_{pl,imp}$ for Alternate Solder at 298K	62
Figure 43.	Plot of $\ln (\sigma_{imp} - \sigma_{0,imp})$ vs $\ln \epsilon_{pl,imp}$ for Alternate Solder at 323K	62
Figure 44.	Plot of $\ln (\sigma_{imp} - \sigma_{0,imp})$ vs $\ln \epsilon_{pl,imp}$ for Alternate Solder at 373K	63
Figure 45.	Plot of $\ln (\sigma_{imp} - \sigma_{0,imp})$ vs $\ln \epsilon_{pl,imp}$ for Alternate Solder at 423K	63
Figure 46.	Plot of E_{imp}^{BISO} vs E for Sn-Ag Solder Using BISO Option	65
Figure 47.	Plot of K_{imp}^{BISO} vs K^{BISO} for Sn-Ag Solder Using BISO Option	66
Figure 48.	Plot of E_{imp}^{MISO} vs E for Sn-Ag Solder Using MISO Option	67
Figure 49.	Plot of $\sigma_{YS,imp}$ vs σ_{YS} for Sn-Ag Solder Using MISO Option	68
Figure 50.	Chart of n_{imp} and n across Various Temperatures for Sn-Ag Solder...	69
Figure 51.	Plot of K_{imp}^{MISO} vs K^{MISO} for Sn-Ag Solder	70
Figure 52.	Chart of m_{imp} and m at Various Strains and Temperatures for Sn-Ag Solder	71
Figure 53.	Chart of $n_{crp,imp}$ and n_{crp} at Various Strains and Temperatures for Sn-Ag Solder	72
Figure 54.	Chart of n_{imp} and n across Various Temperatures for Alternate Solder	73
Figure 55.	Plot of K_{imp}^{MISO} vs K^{MISO} for Alternate Solder	74
Figure 56.	Plot of K_{imp}^{MISO} vs K^{MISO} for Sn-Ag Solder and Alternate Solder Combined	75

LIST OF TABLES

Table 1.	Elastic Properties of Sn-Ag Solder	28
Table 2.	Elastic Properties of Indenter	28
Table 3.	Bilinear Isotropic Properties of Sn-Ag Solder	28
Table 4.	Creep Characteristics of Sn-Ag Solder	28
Table 5.	Multi-linear Isotropic Properties of Sn-Ag Solder	28
Table 6.	MISO Strain versus Stress Values for Sn-Ag Solder	30
Table 7.	σ_{YS} from MISO input stress-strain curve at strain offsets of 0.1% and 0.2% and various temperatures	33
Table 8.	Multi-linear Isotropic Properties of Alternate Solder	36
Table 9.	MISO Strain versus Stress Values for Alternate Solder	37
Table 10.	E^{BISO}_{imp} from BISO Analysis for Sn-Ag Solder at Various Temperatures	43
Table 11.	K^{BISO}_{imp} from BISO Analysis for Sn-Ag Solder at Various Temperatures	43
Table 12.	MISO Impression Stress vs Strain Values for Sn-Ag Solder	44
Table 13.	E^{MISO}_{imp} from MISO Analysis for Sn-Ag Solder at Various Temperatures	47
Table 14.	$\sigma_{YS,imp}$ from MISO Analysis for Sn-Ag Solder at Various Temperatures	47
Table 15.	$\sigma_{0,imp}$, n_{imp} & K^{MISO}_{imp} from MISO Analysis for Sn-Ag Solder at Various Temperatures	50
Table 16.	m_{imp} & $n_{crp,imp}$ for Sn-Ag Solder at Various Temperatures	55
Table 17.	Impression Stress vs Strain Values for Alternate Solder	58
Table 18.	n_{imp} & K^{MISO}_{imp} for Alternate Solder at Various Temperatures	61
Table 19.	Summary of Correlation Factors	77

THIS PAGE INTENTIONALLY LEFT BLANK

ACKNOWLEDGMENTS

I would like to take this opportunity to express my sincerest gratitude to my advisor Professor Indranath Dutta for his patience and understanding in guiding me through this thesis work, which proved to be a journey of self-discovery as well as in-depth learning required for graduate work. Professor Dutta's deep interest and focus on producing good research publications and results have inspired and allowed me to be exposed to the forefront of academia.

Many thanks also to Dr. Deng Pan for bringing me through the initial understanding of finite element modeling of impression testing, as well as Dr. Xin Long, who has provided valuable assistance and insights into the usage of the ANSYSTM software during the whole duration of the research work.

My sincerest thanks also goes out to my sponsor organization Singapore Technologies Engineering who has given me the opportunity to be enrolled in the TDSI course and in turn be part of the remarkable institution of Naval Postgraduate School, of which the experiences and sights I would so dearly miss.

Most importantly of all, I thank God for guiding and allowing me to go through this vigorous training and research work, for His deliverance, and also for providing me my wonderful wife, Joyce, who has so lovingly and encouragingly borne through the relentless nights with me even as I worked to finish up the thesis.

This work was supported by the National Science Foundation (DMR-0209464) and Semiconductor Research Corporation (2002-NJ-1004). The author also gratefully acknowledges the collaboration and assistance of Intel Corporation

THIS PAGE INTENTIONALLY LEFT BLANK

EXECUTIVE SUMMARY

The current method used to obtain mechanical properties of small-sized materials such as Sn-Ag solders is by impression testing since their mechanical properties are inherently different from their bulk samples.

Therefore, impression testing with a flat-tip cylindrical indenter was modeled using a multipurpose finite element code, ANSYSTM, to investigate the correlations between the parameters obtained from impression testing with the mechanical properties of materials obtained from uniaxial testing.

The results show that the elastic modulus can be correlated by a E_{imp}^{BISO}/E ratio of 1.45 using the BISO option and the MISO option gives a E_{imp}^{MISO}/E ratio of 1.44. The simulation gives an $\sigma_{YS,imp}/\sigma_{YS}$ ratio of 2.85 at a strain offset of 0.2% and an $\sigma_{YS,imp}/\sigma_{YS}$ ratio of 2.58 at a strain offset of 0.1%.

The studies also show that the impression strain hardening exponent n_{imp} is related to the uniaxial input strain-hardening exponent by a factor of approximately one. The value of the impression strain-hardening coefficient K_{imp}^{MISO} is related to the uniaxial input strain-hardening coefficient K^{MISO} by an approximate factor of 7.0. The correlation for the strain-hardening coefficient using the BISO option is poor since the curve-fit R-values are low. The simulation studies also included an alternate solder having similar elastic properties but different n and K values for MISO analysis and correlation purposed

The studies show that the impression strain rate hardening exponent m_{imp} is approximately equivalent to the uniaxial input strain rate hardening exponent m. Hence, its reciprocal, the impression creep stress exponent $n_{crp,imp}$ is also approximately equivalent to the uniaxial creep stress exponent n_{crp} .

Therefore, impression testing is the method of choice for testing small-seized materials such as lead-free solders since the parameters obtained from impression testing can be easily correlated to uniaxial test results of which mechanical properties of materials can be easily extracted.

THIS PAGE INTENTIONALLY LEFT BLANK

I. INTRODUCTION

A. MEASUREMENT OF MECHANICAL PROPERTIES

1. Overview

The measurement of mechanical properties of materials has always been important in assisting engineers and metallurgists to determine applications for which the materials are suitable. Accurate measurements of mechanical properties of materials will in part ensure that the materials have been properly tested and qualified so that they are safe for usage in critical applications.

The tensile pull test is probably one of the more conventional methods of testing the mechanical properties of materials. A test specimen is deformed, usually to fracture, with a gradually increasing tensile load that is applied uniaxially along the longitudinal axis of the test specimen. Other common mechanical stress-strain tests include the compression tests, as well as shear and torsional tests.

2. Hardness Testing

The measurement of a material's resistance to localized plastic deformation can be determined through hardness testing. The hardness test normally involves the loading of an indenter made of hard materials, such as tungsten carbide, into the surface of a softer material to be analyzed. The deeper the indentation of the material, the softer the material is and correspondingly, the lower the yield strength of the material.

The hardness test is often described as a non-destructive way of testing materials since the indenter is often small and damage to bulk materials is rare. Hence, it can be routinely used for batch tests on small samples of materials to ascertain their yield specifications. The normal method used in obtaining hardness values is to measure the depth or area of an indentation impressed by a punch of definite shape for a defined period of time with a specified force. The

commonly used hardness tests include the Rockwell Hardness Test, Brinell Hardness Test, and Knoop and Vickers Microhardness Tests [1].

The Rockwell hardness test involves the usage of a diamond cone or hardened steel ball indenter to indent the test sample. The Rockwell hardness number is obtained from calculations based on the permanent increase in penetration depth resulting from the application and removal of a large load.

The Brinell hardness test involves the usage of a hardened steel or carbide ball to indent the test sample. A low powered microscope is typically used to obtain the indentation diameter that is impressed on the test sample. The Brinell number is subsequently calculated by dividing the applied load with the area impressed on the test sample.

The Vickers hardness test involves the usage of a square based pyramid to indent the test sample and it is one of the more frequently used tests for hardness measurements. The Vickers hardness number is obtained from calculations based on the applied load and the impressed area of the test sample.

These test methods are still widely viable for usage especially in bulk samples, but the move towards miniaturization of mechanical components brought about new challenges and interests in indentation techniques and these are discussed below.

B. APPLICATIONS OF INDENTATION TECHNIQUES

1. Micro-Electro-Mechanical Systems Challenges

The rapid miniaturization of microelectronic devices and micro-electro-mechanical systems (MEMs) has resulted in increasing interest in microelectronics packaging. Microelectronics and MEMs devices are widely used in several critical applications in the military such as unmanned aerial vehicles (UAVs) as well as modern computational instruments for both medical as well as design purposes.

One of the main challenges faced in microelectronics packaging is the high failure of the microelectronic solder joints during service applications. These joints are usually exposed to severe thermo-mechanical cycling while in service. The thermal expansion mismatch between the silicon chip and the substrate will potentially result in low-cycle fatigue failure.

Hence, the mechanical properties of the solder material are important in determining the performance and durability of flip-chip and ball grid array solder joints. Significant interest has been developed on establishing approaches to accurately determine the mechanical properties of these micron-sized solder balls. This is because their material properties are extremely difficult to characterize through conventional test methods mentioned earlier. Therefore, the technique commonly used to characterize the material properties of these solder balls is instrumented impression testing, where a probe is used to indent the test specimen.

Impression testing is attractive because it allows a micron to nano-sized non-destructive test capability. It also removes the need for hardness impression imaging. Moreover, it may be difficult to extract solder ball joints and engineering welds for uniaxial testing and hence impression testing becomes the method of choice in which to extract material properties for these small structural features.

In addition, creep tests performed via impression testing are able to establish steady state within very short times. The mechanical behavior of bulk solder joint samples and small solder ball joints are significantly different. Hence, impression testing becomes a relevant technique to determine behavior and properties of thin films and small structural features. The mechanical behavior and properties of these materials at small scale can then be determined from load and displacement measurements.

2. Thin Films

Impression testing can also be applied to determine the mechanical properties of thin films on substrates. Thin film coatings are currently been widely

used to extend the performance and durability of machine parts. The indentation response of thin films on substrates is a complex function involving the elastic as well as plastic properties of both the film and the substrate. Current methods to extract properties from load-displacement data are mostly suitable for monolithic materials only. Hence, a widely accepted engineering approximation is to limit the indentation depth to less than 10% of the film thickness, which is feasible only for thin films that are about a micrometer thick.

Therefore, there is a need to use both new experimental and theoretical methods to extract “true” film properties from nano-indentation of film/substrate composites. Saha and Nix [13] have performed experiments to measure the contact stiffness during indentation, and together with the known elastic modulus of the system, the true contact area and hardness can be determined irrespective of the effects of pile-up or sink-in around the indenter.

The development of impression testing will be further described in the literature review in Chapter II.

II. LITERATURE REVIEW

A. HISTORY OF IMPRESSION TESTING

The theory of using impression testing to extract mechanical properties of materials can be attributed way back to analytical solutions proposed by Hertz [16] who assumed paraboloids in elastic contact, as well as Boussinesq's [16] computational methods based on potential theory to obtain solutions to the case of penetration by a solid of revolution whose axis was normal to the original boundary of the half space. Boussinesq's [16] methods only resulted in partial numerical results for the cases of a flat-ended cylindrical punch and a conical punch.

Subsequently, Harding and Sneddon [2] used the theory of Hankel transforms to express the axisymmetric solution of the equations of elastic equilibrium in terms of Hankel transforms in order to obtain expressions for D , the total depth of penetration of the punch tip, and for P , the total punch load in terms of the radius a of the contact circle between the punch and the elastic solid. Hence, expressions were obtained for special cases of impression with specific indenter geometries such as the rigid conical punch, rigid sphere and the flat-ended cylindrical punch. The expressions are as follows:

For a rigid conical punch:

$$P = \frac{\pi E}{2(1 - \sigma^2)} a \varepsilon \quad (1)$$

For a rigid sphere:

$$P = \frac{4E}{3(1 - \sigma^2)} \frac{a^3}{R} \quad (2)$$

For a flat-ended cylindrical punch:

$$P = \frac{2}{1 - \sigma^2} E \varepsilon a \quad (3)$$

Nevertheless, the solutions are unable to express D and P in terms of an arbitrary constant f due to the complexity of the dual integral equations. Sneddon [3] then used an elementary solution to resolve the complexity and obtained formulae for special shapes of punch.

For a flat-ended cylindrical punch:

$$P = \frac{4\mu a D}{1-\eta} \quad \text{where } \mu = \text{rigidity modulus}, \quad (4)$$

$\eta = \text{poisson ratio}$

$$\mu = \frac{E}{2(1+\eta)}$$

For a conical punch:

$$P = \frac{\pi\mu a^2}{1-\eta} \tan \alpha \quad \text{where } \alpha = \text{semivertical cone angle} \quad (5)$$

For a punch in the form of a paraboloid of revolution:

If the paraboloid of revolution has equation $\rho^2 = 4kz$

$$P = \frac{8\mu}{3(1-\eta)} \sqrt{(2kD^3)} \quad (6)$$

For a spherical punch:

Taking $f(x) = R - \sqrt{R^2 - a^2x^2}$ where sphere is of radius R and elastic solid is circle of radius a ,

$$P = \frac{\mu}{1-\eta} \left\{ (a^2 + R^2) \log \frac{R+a}{R-a} - aR \right\} \quad (7)$$

For a punch in the shape of an ellipsoid of revolution:

Taking $f(x) = \alpha \{1 + \sqrt{1 + a^2x^2/\beta^2}\}$ where α and β are semi-axes of the ellipsoid of revolution

$$P = \frac{\mu\alpha}{(1-\eta)\beta} \left[(\alpha^2 + \beta^2) \log \frac{\beta + \alpha}{\beta - \alpha} - 2\alpha\beta \right] \quad (8)$$

The above formulae present well-defined solutions for the elastic regime within the classical theory of elasticity. However, elastic-plastic properties of materials remained as a great challenge for scientists and researchers since analytical solutions for plasticity in impression testing is not easily obtained due to nonlinearity in constitutive equations, as well as the need for material parameters such as work hardening coefficients to describe material behavior.

Johnson [4] hypothesized that Hill's [5] analysis for the expansion of a spherical cavity in an elastic-plastic material could be applied to the hemispherical radial modes of deformation commonly found in impression testing. This is achieved by replacing the cavity with an incompressible hemispherical core of material beneath an indenter radius equivalent to the contact circle. The core is hence surrounded with a hemispherical plastic zone that connects with the elastically strained material at a larger radius. The volume of material displaced by the indenter during the impression test leads to high stresses that can cause plastic deformation in the surrounding material, hence giving rise to the formation of a plastic zone. However, the conclusions drawn from the analytical solutions are restricted to elastic and perfectly plastic solids that have a constant yield stress in compression and cannot be applied to materials with strain hardening behavior.

Tabor [6] is probably one of the pioneers in using load and displacement sensing indentation methods to measure mechanical properties of materials. The well-documented "Hardness of Metals" by Tabor [6] describes the methodology for hardness measurements by spherical, conical as well as pyramidal indenters. The hardened spherical indenter was used to study the mechanical properties of several metals.

Tabor [6] further correlated the hardness of a metal with its elastic limit, and with the way in which the elastic limit varies with the deformation to which the metal has been subjected. He found that Hencky [6] has obtained an approximate solution to Mises's equation for two-dimensional plasticity in the case of a frictionless cylindrical punch penetrating an ideally plastic solid. Plastic

yielding occurs when the mean punch pressure P_m is about 2.8 times the yield stress Y of the material. Ishlinsky [6] performed his analysis for the case of a spherical punch penetrating an ideally plastic solid and found that P_m is about 2.6 Y . Hence, it can be clearly inferred that for a first approximation, plastic yielding occurs when

$$P_m = cY \quad (9)$$

where c is a constant of value approximately equals to three.

The above derivations hinges on the assumption that frictional effects between the face of the indenter and the metal sample is negligible so that the metal is perfectly free to slip laterally at the interface during the indentation process. Hence, the pressure is uniform across the face of the indenter and has a value of about 3 Y . If however there are significant frictional forces between the surfaces, there will be an increase in pressure needed for indentation. Since the metal sample is more confined in the center compared to the edges of the indenter, the pressure forces will be higher in the center than at the edges. Hence, the flow pattern will be modified and the yield stress would also be higher. The mean pressure across the surface of the indenter may be approximated as

$$P_m = P_0 \left(1 + \frac{\mu a}{h} \right) \quad (10)$$

where P_0 is the pressure necessary to produce plastic yielding, μ is the friction coefficient, h is the thickness and a is the width. If $h = a$ and $\mu = 0.2$, $P_m = 1.2P_0$. Hence, the mean pressure at which plastic yielding occurs may be increased by about 20% for reasonable friction coefficients. In the case of a flat tip indenter penetrating a metallic surface, the effects of friction will probably be of the same order of magnitude and the pressure at which the indenter begins to penetrate the surface will not be more than a few percent greater than the theoretical value of 3 Y .

Further experiments performed by Stillwell and Tabor [7] revealed that there is little change in the indenter diameter during withdrawal of the indenter but rather a decrease in its depth. These experiments revealed that if the shape of the perturbed surface in elastic analysis is taken into account, plasticity effects on elastic unloading data can be investigated. Tabor [8] showed that the shape of the unloading curve and the total amount of recovered displacement can be related to the elastic modulus, as well as the size of the impression for both the spherical and conical indenters.

It is also shown that when a hard spherical punch is pressed on to the plane surface of an ideally plastic body, the region of contact is a circle of radius a given as

$$a = \left[\frac{3}{4} Wgr \left(\frac{1 - \sigma_1^2}{E_1} + \frac{1 - \sigma_2^2}{E_2} \right) \right]^{\frac{1}{3}} \quad (11)$$

where W is the applied load, E_1 and E_2 are the elastic modulus of the indenter and metal sample respectively, and σ_1 and σ_2 are the corresponding values of Poisson's ratio. The Poisson's ratio of most metals has a value of about 0.3 and this result in

$$a = 1.1 \left[\frac{Wgr}{2} \left(\frac{1}{E_1} + \frac{1}{E_2} \right) \right]^{\frac{1}{3}} \quad (12)$$

Hence, the projected area A of the indentation is proportional to $W^{2/3}$ and the mean pressure P_m over the contact region is proportional to $W^{1/3}$. The pressure across the contact circle is non-uniform and the pressure at any point distance x from the center of the indentation is given as

$$P = P_0 \left(1 - \frac{x^2}{a^2} \right)^{\frac{1}{2}} \quad (13)$$

where P_0 is the pressure at the center of the contact circle and so it can be determined that

$$P_0 = \frac{3}{2} P_m \quad (14)$$

The Mises' criterion will indicate that the material of the body exceeds the elastic limit when P_m is about $1.1Y$. The deformation remains completely elastic provided the mean pressure is less than $1.1Y$. The surface and the indenter return to their original shape on load removal but as soon as P_m reaches $1.1Y$, plastic deformation occurs. As the load is increased, the plastic region grows until the whole material around the indentation is in a state of plasticity. At this stage, P_m is approximately $3Y$. The transition in P_m from $1.1Y$ to $3Y$ is due to plastic deformation that is distinct from work-hardening effects.

The relationship between loading and size of indentation for spherical indenters may also be expressed by Meyer's law, which states that for a ball of fixed diameter, if W is the load and d is the chordal diameter of the remaining indentation, then

$$W = kd^n \quad (15)$$

where k and n are material constants to be determined. The value of n is generally greater than 2 and for completely unworked materials, n has a value near to 2.5 while for fully work-hardened materials, the value is close to 2. Log-log plots of the above equation are plotted and the slope is numerically equivalent to the Meyer index n while the value of W at which d is equal to 1 is numerically equivalent to k . Tabor's [6] tests on several work-hardened metals reveal that at very small loads where the deformation is essentially elastic, the Meyer index will have an upper value of about 3. At higher loads, the index will decrease until it approaches the constant value characteristic of the state of work hardening of the metal.

It should be noticed that the indenter in impression testing has the possibility to be permanently deformed. For soft metallic samples, the indenter would only deform elastically but permanent deformation may occur if harder metals are impressed. Suppose that a metal has a yield pressure at full plasticity of B described by

$$B \sim 2.8Y \quad (16)$$

and the indenter has the corresponding correlation given by

$$B_i \sim 2.8Y_i \quad (17)$$

As the load of the indenter is increased, plastic deformation of the metal will begin to occur at a mean pressure of approximately $1.1Y$. Considering the fact that $Y_i > Y$, this pressure would be less than $1.1Y_i$, so that the stress will be insufficient to produce any plastic deformation of the indenter. As the load is increased, the mean pressure between the indenter and the metal sample increases until it reaches a value of about $2.8Y$. If therefore the pressure is not to be sufficient to produce even the onset of plastic deformation of the indenter, it must be less than $1.1Y_i$. This implies that $2.8Y < 1.1Y_i$ or $Y_i > 2.5Y$ or $B_i > 2.5B$. These simply state that the indenter should be at least 2.5 times as hard as the samples under testing.

B. CURRENT INTEREST IN IMPRESSION TESTING

Probably, most of the current interest in impression testing stems from the instrumented indentation techniques developed by Oliver and Pharr [9], as well as creep testing via a flat punch indenter by Chu and Li [10]. Instrumented indentation or 'load-depth sensing' indentation primarily consists of a controlled load P applied through an indenter tip that is in contact with a test sample. The penetration depth h_s of the indenter tip into the material is recorded as a function of the applied load.

The recent push towards nanotechnology transpired the need for nano-indentation techniques [11] and studies [12, 13] to probe mechanical properties of nano-materials. The modulus and the hardness can be extracted during the initial portions of the unloading curve. Some common geometrical types of indenters include the following:

Three-sided pyramid Berkovich indenter – The Berkovich indenter has an area-to-depth function similar to that of the Vicker's indenter.

Conical indenter – The conical indenter has a similar geometry to the Berkovich. It has a simple cylindrical symmetry and does not have stress concentrations associated with the sharp edges of the pyramid indenters.

Spherical indenters – The spherical indenter does not produce elastic singularity at the tip of the indenter. Deformation at small loads and displacements is entirely elastic and transforms to plastic deformation at higher loads and displacements.

The flat-ended circular punch indenting a half-space yields a solution

$$S = \frac{dP}{dh} = \frac{2}{\sqrt{\pi}} E_r \sqrt{A} \quad (18)$$

and

$$\frac{1}{E_r} = \frac{1-\nu^2}{E} + \frac{1-\nu_0^2}{E_0} \quad (19)$$

where $S = dP/dh$ is the experimentally measured stiffness of the unloading data and E_r is the reduced modulus. A is the projected area of the elastic contact, P is the load, h is the penetration depth, E and ν are elastic modulus and Poisson's ratio for the specimen, and E_0 and ν_0 are the same parameters for the indenter. The modulus can thus be computed by measuring the initial unloading stiffness and assuming that the contact area is equal to the optically measured area of the hardness impression.

Fisher–Cripps [14] showed that the use of the reduced modulus E_r as described above is valid for impression test data. Since only the slope or unloading stiffness is used, the explicit accommodation of the indenter deflection does not have any consequential effect than if it was transferred to that within the test sample by artificially reducing the sample modulus to become the reduced modulus E_r .

Bhattacharya and Nix [15] followed up with an empirical method to evaluate the projected contact area. The solution is based upon the extrapolation of the initial portion of the unloading curve to zero load and subsequently using

the extrapolated depth with the indenter shape function to determine the contact area. Pharr, Oliver and Brotzen [16] also showed that the equations described above are applicable to any indenter that can be described as a body of revolution possessing a smooth function.

It was subsequently revealed by Oliver and Pharr [9] that the above equations may apply to indenters of other geometries and King [17] showed by finite element analysis that the solution may be put in the form

$$S_0 = \beta E_r \sqrt{A} \quad (20)$$

where A is the contact area, and β is a numerical factor giving values for the following geometrical shapes:

$$\text{Circle} - \beta = 1.129; \quad (21)$$

$$\text{Square} - \beta = 1.142; \quad (22)$$

$$\text{Triangle} - \beta = 1.167; \quad (23)$$

Doerner and Nix [18] approached hardness and modulus measurements based on observations that the elastic behavior of the indentation contact is similar to that of a flat cylindrical punch during the initial stages of unloading. They suggested that the initial portions of the unloading curves are linear, and the area of contact remains constant as the indenter is unloaded. Hence, the hardness can be computed from

$$H = \frac{P_{\max}}{A} \quad (24)$$

where P_{\max} is the peak indentation load and A is the projected area of the hardness impression.

Contrary to the assumption of linearity in unloading curves by Doerner and Nix [18], Oliver and Pharr [9] used the Berkovich indenter to reveal that the unloading curve can be described by the power law relation

$$P = A(h - h_f)^m \quad (25)$$

where P is the load, $(h - h_f)$ is the elastic displacement, and A and m are material constants. The variation of the power law exponents from $1.2 < m < 1.6$ shows the non-linearity of the unloading curves and suggests that the indenter appears to behave more like a paraboloid of revolution.

These derived equations work well for pure elastic contact but its robustness in analysis of elastic-plastic deformation is questionable. Elastic solutions fail to accurately capture the effects of pile-up and sink-in of material around the indenter in elastic-plastic deformation. Materials are assumed to always sink-in for pure elastic contact solutions whereas they may either sink-in or pile-up for elastic-plastic contact solutions.

Bolshakov and Pharr [19] investigated the effects of pile-up on the determination of the elastic modulus and observed that when pile-up is large, the load-displacement curves underestimate the true contact areas. Hence, the properties of hardness and elastic modulus tend to be overestimated. Since the parameter h_f/h_{max} can be measured experimentally, it can be used as a means to indicate whether the effects of pile-up are significant. Pile-up effects are typically significant when h_f/h_{max} is greater than 0.7 and also provided that the material does not work harden appreciably. For materials that only work harden moderately, pile-up is not considered significant and this occurs when h_f/h_{max} is smaller than 0.7. In this instance, Oliver and Pharr's [9] analytical methods can be deemed sufficient to give reasonable results.

In addition, Hay, Bolshakov, Pharr [20], and Wolff [21], recommended the inclusion of a correction factor β to the stiffness equation to give

$$S = \frac{dP}{dh} = 2\beta E_r \sqrt{\frac{A}{\pi}} \quad (26)$$

where S is the experimentally measured stiffness of the upper portion of the unloading data, E_r is the reduced modulus, and A is the projected area of the elastic contact. The correction factor is used to account for the boundary conditions that allow inward displacement of the surface. Hence, the elastic modulus can be determined as

$$E = \frac{(1-\nu^2)}{2\beta} \sqrt{\frac{\pi}{A}} \frac{dP}{dh} \quad (27)$$

The correction factor β for a conical indenter with half apex angle γ less than 60° is given as

$$\beta = 1 + \frac{2(1-2\nu)}{4(1-\nu)\tan\gamma} \quad (28)$$

and that for larger cone angles such as the Berkovich indenter is given as

$$\beta = \pi \frac{\frac{\pi}{4} + 0.155 \cot\gamma \frac{1-2\nu}{4(1-\nu)}}{\left[\frac{\pi}{2} - 0.831 \cot\gamma \frac{1-2\nu}{4(1-\nu)} \right]^2} \quad (29)$$

The correction factor β for a spherical indenter is given as

$$\beta = 1 + \frac{2(1-2\nu)a}{3\pi(1-\nu)R} \quad (30)$$

where a is the contact radius and R is the radius of the spherical indenter.

Since the mechanical properties of materials can be easily obtained from uniaxial stress-strain curves, the important factor to consider in impression testing is to establish relationships between the uniaxial stress-strain curves and impression test data.

Dao and Suresh [22] embarked on finite element modeling to investigate these relationships by using the load-displacement curve responses of a conical indenter to evaluate the elastic-plastic properties of a combination of materials. They defined three variables from the load displacement curve given as

$$C = \frac{P}{h^2} \quad (31)$$

$$S = \frac{dP}{dh} \quad (32)$$

$$\frac{h_r}{h_m} \quad (33)$$

where C is the loading curvature, S is the stiffness of the initial loading and h_f/h_m is the ratio of the residual depth to the maximum depth. Subsequently, they obtained analytical expressions from the FEM results and hence were able to relate the indentation data to elastic-plastic properties of the materials. However, it was found that the plastic properties of the materials are strongly affected by even small variations in the extracted parameters from the impression test data.

Nevertheless, Cheng and Cheng [23] claimed that it is quite possible to obtain resembling load displacement curves from impression testing for different material properties. However, it is quite unknown whether it is feasible to extract stress-strain curves from load displacement curves alone since this may not be an accurate representation of the elastic-plastic response.

Giannakopoulos and Suresh [24] also devised a methodology using instrumented sharp indentation to determine elastic-plastic properties of materials. The method removes the need to measure the impression area and allows for unique correlations between the impression depth h and the true impression area A for commercially sharp indenters. In addition, the method also accounts for pile-up and sink-in. The methodology also characterizes an equivalent plastic strain that separates different modes of plastic deformation under the sharp indenter, which is very similar to the cavity model proposed by Johnson [4]. The inner region consists of a zone where the material is punched by the sharp indenter while the surrounding region consists of a zone of strong plastic strains that is engulfed by an elastic-plastic regime. It is in this regime that Johnson's cavity model [4] can be applied to extract the hemispherical elastic-plastic boundary. Hence, the work of Giannakopoulos and Suresh [24] can be pinpointed to the devised characteristic plastic strain that is used to determine the mechanical properties of materials by sharp indentation.

Apart from the Oliver and Pharr [9] method that utilizes sharp indentation, another popular method to determine hardness and elastic modulus of materials is the Field and Swain [25] method that utilizes the spherical indenter. Although different parameters are considered in the determination of the elastic modulus

for both methods, it was found that both methods essentially have similar contact mechanics analyses. The method of Field and Swain [25] considers both the elastic and plastic regions during a spherical indent by assuming a flat, smooth, isotropic material, as well as an orthogonal indenter and material contact. The spherical indenter will firstly induce an elastic response, and subsequently a plastic response with increasing load. Fracture will eventually occur around the impression for brittle materials. For a completely elastic response, it is shown by Johnson [4] that the reduced elastic modulus is given by

$$E_r = \frac{3P}{4ah_e} \quad (34)$$

where h_e is the elastic penetration depth and a is the contact radius between the indenter and the test sample. Hence, there is a need to determine h_e and a only since the loading can be directly measured. The main assumption made in both of these indentation methods is that the initial part of the unloading curve is equivalent to a completely elastic response. The relation for the total penetration depth through the whole loading and unloading process is given as

$$h = h_r + h_e \quad (35)$$

which simply states that the total penetration depth consists of elastically recoverable and residual depth. Alternatively, h is also given as

$$h = h_c + \frac{h_e}{2} \quad (36)$$

which is based on the defining the total depth as the contact depth plus the elastic surface deflection. Johnson [4] also showed that the load-displacement relationship for the elastic contact of a spherical indenter on a flat surface is given as

$$P = Ch_e^{\frac{3}{2}} \quad (37)$$

where C is a constant that is dependent on material properties. If the residual component of the total depth h_r is neglected upon unloading, the change in the

total penetration h with respect to P will be due to the elastic loading only, and may be described by the equation above. Hence, the relationship

$$\left(\frac{P_m}{P_p}\right) = \left(\frac{h_m - h_r}{h_p - h_r}\right)^{\frac{3}{2}} \quad (38)$$

can be deduced where the subscript m refers to a point of maximum load and displacement and subscript p refers to a point of partial unloading of the material. The radius of the contact circle can be calculated from geometry and is given as

$$a = \sqrt{2Rh_c - h_c^2} \quad (39)$$

where R is the radius of the indenter. However, the determination of the hardness of a material using the spherical indenter is more involved as compared to using a Berkovich or a sharp indenter. This is because a spherical indenter does not induce plasticity on most materials instantly, thus requiring an indentation that attains a depth where full plastic flow is developed. For metals, this is attained when the impression stress is about three times the yield stress of the material.

On the other hand, Alcalá, Barone and Anglada [26] chose to study the surface deformation mode during impression testing instead of solely relying on load-displacement data to obtain the stress-strain curves. In their work, they found that the phenomenon of sink-in is prevalent in materials where the strain hardening exponent n is greater than 0.2. It was concluded that surface deformation modes influence the measurements of both hardness and elastic modulus since the true impressed area increases when the phenomenon of pile-up is prevalent and decreases when sink-in occurs instead. If the surface deformation modes of pile-up and sink-in are not taken into account, there can be large errors incurred in the computation of the impressed area. Alcalá etc [26] quantified the pile-up and sink-in around the spherical indenter by the equation

$$h = h_s c^2 \quad (40)$$

where h_s is the maximum penetration depth beneath the initial surface and h describes the location of the impressed area. A parameter c^2-1 was used to determine the amount of pile-up and sink-in. If the parameter is greater than zero, pile-up occurs and if the parameter is less than one, sink-in occurs. The factor c^2 is deemed to be a function of the strain hardening exponent n and it is also described by the equation given as

$$c^2 = \left(\frac{\frac{2}{n} - 1}{\frac{4}{n} + 1} \right) \left(\frac{4s + 1}{2s} \right) \quad (41)$$

where s is a dimensionless parameter that depends on the pressure distribution over the impressed surface.

Besides the advances in indentation techniques to measure hardness and modulus, great strides were made by Chu and Li [10] in creep testing using impression testing as well. They introduced an indenter that is a circular cylinder with a flat end. Steady state velocity is rapidly observed in this new test method after a transient period during which an impression is made on the specimen. It was found that the steady-state velocity could be correlated to similar stress and temperature dependencies in unidirectional creep tests using bulk samples. Chu and Li [10] performed impression creep on succinonitrile crystals and found that there are three possible mechanisms for impression creep of single crystals namely bulk diffusion, surface diffusion and dislocation creep. The impression velocity was found to be proportional to the punch stress while a power law constitutive equation given by

$$\dot{\epsilon}_e = A \sigma_e^n \quad (42)$$

was observed, where $\dot{\epsilon}_e$ is the unidirectional creep rate, σ_e is the unidirectional stress, and A and n are constants at constant temperature. The impression velocity can be defined by the expression

$$v_d = 2Aa(\sigma/m)^n \quad (43)$$

where a is the punch radius and m is a factor related to hardness/strength ratios, which was found to be 3.3 in experiments.

Yu and Li [27] supplemented the experiments by Chu and Li [10] with a finite element analysis of impression creep of the same conditions and found that for succinonitrile crystals, the impressing velocity at steady state conditions agree very well with the experiments. Hence, a power law between the steady state impression velocity and the punch stress can be established due to the power law assumption between steady state creep and Von Mises stress for each finite element.

It can be seen that impression creep tests are of great value since it enables one to obtain extensive creep information from limited supply of materials. All the tests can be carried out in one sample, which reduces sample preparation time as well as sample to sample variation in preparation and testing. The possibility of characterizing local material properties is also of great benefit.

Subsequently, more studies were conducted using impression creep. Yang and Li [28] performed impression creep and stress relaxation experiments on Sn-Pb eutectic alloys. The creep properties of the Sn-Pb eutectic alloy is already very well-documented and the temperature influence on the deformation rate is dominated by the exponential dependence which can be expressed as

$$\dot{\epsilon} = A \sigma^n \exp(-Q / RT) \quad (44)$$

where A is a constant, n is the stress exponent, Q is the activation energy, R is the gas constant and T is the absolute temperature. Yang and Li [28] found that the stress dependence could be described by a hyperbolic sine function of stress for all stresses and temperatures studied. A single mechanism of interfacial viscous shear flow was proposed for both creep and stress relaxation. Yang, Li and Shih [29] also performed a computational simulation of impression creep using the hyperbolic sine stress law to supplement their experimental work.

Yang, Chen, Seidmann and Li [30] investigated punch tip effects in diffusional creep by using a cylindrical punch with a semi-spherical tip and

comparing the impression velocity with that of the flat tip and found that the impression velocity of the former is $4/\pi$ faster than the latter. They also found that for a cylindrical punch with a flat tip, the effect of depth is not so significant if the lateral contact area is a free surface, but it can be appreciable if the lateral contact area is impermeable to vacancies.

Yang [31] also used a finite element method to study the effects of slip, stick and cavity depth on impression creep and found that there is a well-defined steady punch velocity after a transient stage that increases with the stress exponent, but decreases with increasing cavity length. The steady punch velocity is the largest for all slip condition and the smallest for both the lateral stick and all stick conditions.

Balani and Yang [32] used impression testing to study the creep behavior of 90 Pb-10 Sn alloy and obtained a stress exponent of 4.3 and a creep activation energy of 46.7 KJ/mole for their set of experimental conditions.

Rani and Murthy [33] studied the impression creep behavior of tin based lead free solders and found that the impression creep curves are all similar to conventional creep curves with steady state attained after a transient period. They also found a power law behavior displayed by the alloys with stress exponents ranging from 2 to 6.3. Tin based lead free solders are better than conventional solders because there are less toxic effects.

Hence, there is an increasing interest in lead free solders and the approaches to accurately characterize their material behavior. Pan, Marks, Dutta, Mahajan and Jadhav [34] set up a facility to test ball grid array solder balls using miniaturized impression creep apparatus. Pan and Dutta [35] also investigated the mechanics of impression creep testing as applied to Sn-3.5Ag solder using finite element analysis and found that the test times could be substantially shortened if plastic deformation is applied to the sample surface prior to the testing.

Hence, it can be seen that impression testing can be very effective in the study of miniaturized components such as Sn-Ag solders. The ability to relate

impression tests to conventional compression tests will enable stress-strain relations to be easily determined since there already exists a large amount of information for compression tests. Hence, the impetus of this thesis is to look into some of the correlations between impression testing and compression testing in the determination of mechanical properties of Sn-Ag solders.

C. OBJECTIVE AND SCOPE

1. Elastic Properties

Harding and Sneddon [2] had shown that the relationship between the impression stress P_m and the penetration depth δ below the free surface is given by

$$P_m = \frac{4E}{\pi(1-\nu^2)} \left(\frac{\delta}{D} \right) \quad (45)$$

where E is the elastic modulus and ν is the Poisson's ratio. The penetration depth is normalized with the indenter diameter D to give non-dimensional strain, as well as indenter geometry independence. In addition, the impression elastic modulus E_{imp} is related to the uniaxial elastic modulus E by the equation given as

$$E_{imp} = \frac{4}{\pi(1-\nu^2)} E \quad (46)$$

and this has been investigated by Yu, Imam and Rath [36] for some materials such as aluminum, copper, nickel and mild steel.

Hence, the first objective of this FEM study is to verify the relationship from equation (46).

2. Plastic Properties

The yield strength is generally defined as the stress at which plastic deformation takes place and is important in determining the strength of the material. The relationship between the impression yield strength $\sigma_{YS,imp}$ and the uniaxial yield strength σ_{YS} has been described by Tabor [6] as having a factor of three and this relationship will be investigated.

In addition, the material's capacity for plastic deformation by strain hardening may also be investigated by impression testing and one of the more common definitions of the stress-strain relationship from the onset of yielding to the maximum load may be described by Hollomon's equation [37]

$$\sigma = \sigma_0 + K \varepsilon_{pl}^n \quad (47)$$

where σ is true stress, σ_0 is the proportional limit, ε_{pl} is true plastic strain, n is strain-hardening exponent and K is the strain-hardening coefficient defined as the true stress at a true strain of 1.0.

Taking the logarithm on both sides of the above equation, the impression stress and strains can be described by the relationship

$$\ln(\sigma_{imp} - \sigma_{0,imp}) = n_{imp} \ln \varepsilon_{pl,imp} + \ln K_{imp} \quad (48)$$

Hence, the slope of the graph is the strain hardening exponent n_{imp} and the intercept is $\ln K_{imp}$.

Therefore, the relationship between the impression strain-hardening coefficient K_{imp} , which can be obtained from the graphical plot of equation (48), and the uniaxial strain-hardening coefficient K , which is the input, will be investigated. The impression strain-hardening exponent n_{imp} can be similarly obtained and the relationship with the uniaxial strain-hardening exponent n will be investigated.

3. Creep Properties

The standard creep equation is given as

$$\dot{\epsilon} = A_1 \left(\frac{Gb}{kT} \right) \left(\frac{\sigma}{G} \right)^{n_{crp}} e^{\frac{-Q}{RT}} \quad (49)$$

Based on equation (49), it is possible to obtain a strain rate hardening law [1] given by

$$\sigma \propto C \dot{\epsilon}_{pl}^m \quad (50)$$

where C is the strain-rate hardening coefficient and m is the strain-rate hardening exponent. Correspondingly, by taking logarithm on both sides of equation (50), the impression stress and plastic strain rate can be described by the relation

$$\ln \sigma_{imp} = \ln C_{imp} + m_{imp} \ln \dot{\epsilon}_{pl,imp} \quad (51)$$

where m_{imp} is the impression strain-rate hardening exponent and C_{imp} is the impression strain-rate hardening coefficient.

The strain-rate hardening exponent m is a parameter that is related to the creep stress exponent n_{crp} , by the relationship

$$n_{crp} = \frac{1}{m} \quad (52)$$

Therefore, the impression creep stress exponent $n_{crp,imp}$ can be similarly obtained by substituting m with m_{imp} in equation (52).

Hence, the final objective of the FEM study is to find out the relationship between m_{imp} and m , and correspondingly the relationship between $n_{crp,imp}$ and n_{crp} .

The methodology for the various FEM simulation studies will be described in Chapter II.

III. METHODOLOGY

A. FINITE ELEMENT MODELING

1. Overview

Analytical solutions to characterize the elastic behavior of materials are readily available, but the plastic characterization of materials is more complex. Modeling of impression tests that includes plasticity can be difficult and subjective since the constitutive equations are inherently non-linear and several material parameters, such as the yield strength and work hardening coefficient, must be included in the analysis. Hence, analytical solutions are not easily obtained [4].

Therefore, finite element modeling can be used to simulate and include the effects of plasticity but these can be subjected to inaccuracies caused by inadequate meshing and convergence. Nevertheless, finite element simulations have been frequently used to analyze creep in impression tests, and since mechanical properties of materials can be obtained from experimental testing, it is also possible to obtain mechanical properties of materials from computational simulation to a reasonable degree of accuracy.

2. Model Description

In this computational simulation, the finite element software ANSYSTM is used to investigate the impression testing of the Sn-Ag solders.

The Sn-Ag solder is simulated in a 2-D half-space as an axisymmetric problem. The solder was assumed to be a cylinder of diameter 10mm and height 5mm. The indentation probe was modeled as a punch having a diameter of 1mm, as well as a fillet radius of 0.5 μ m so as to avoid singularities at the indenter corner.

The indenter was assumed to be non-deformable and meshed using 2-D triangular axisymmetric elements (Plane 82), which gives the required stiffness. The surface between the indenter and the solder surface was modeled using

contact elements, with the indenter sides being picked as target (Target 169) and the solder surface being picked as contact (Contact 172). The solder was meshed with 2-D 8-noded axisymmetric elements (Plane 183).

The boundary conditions that were applied to the model are:

$$u_{\theta} = 0 \text{ for all nodes}$$

$$u_z = 0 \text{ for all nodes at the bottom of the solder}$$

$$u_r = 0 \text{ for all nodes along the axisymmetric axis}$$

A displacement of 0.05 mm was applied to the top surface of the indenter to simulate the impression of the solder so that a constant normalized strain rate of $5E-2$ is applied. The solder was initially modeled using bi-linear isotropic plastic hardening properties, where the strain-hardening exponent n is assumed to be one, and later modeled using multi-linear isotropic plastic hardening properties, where the strain-hardening exponent n is typically for Sn-Ag solders.

In order to investigate the strain rate effects in impression testing, properties for steady-state creep via a power-law relation given by equation (49) are used. The normalized strain rates used were $5E-4$, $5E-5$ and $5E-6 \text{ min}^{-1}$, which were achieved by inputting a displacement of 0.05 mm over 6000, 60000 and 600000 seconds respectively.

The impression tests were simulated over a range of temperatures from 298K to 423K. The punch stress was extracted from the top surface of the indenter while the penetration depth was obtained from the displacement of the bottom of the indenter, and these were to be used for the stress-strain analyses.

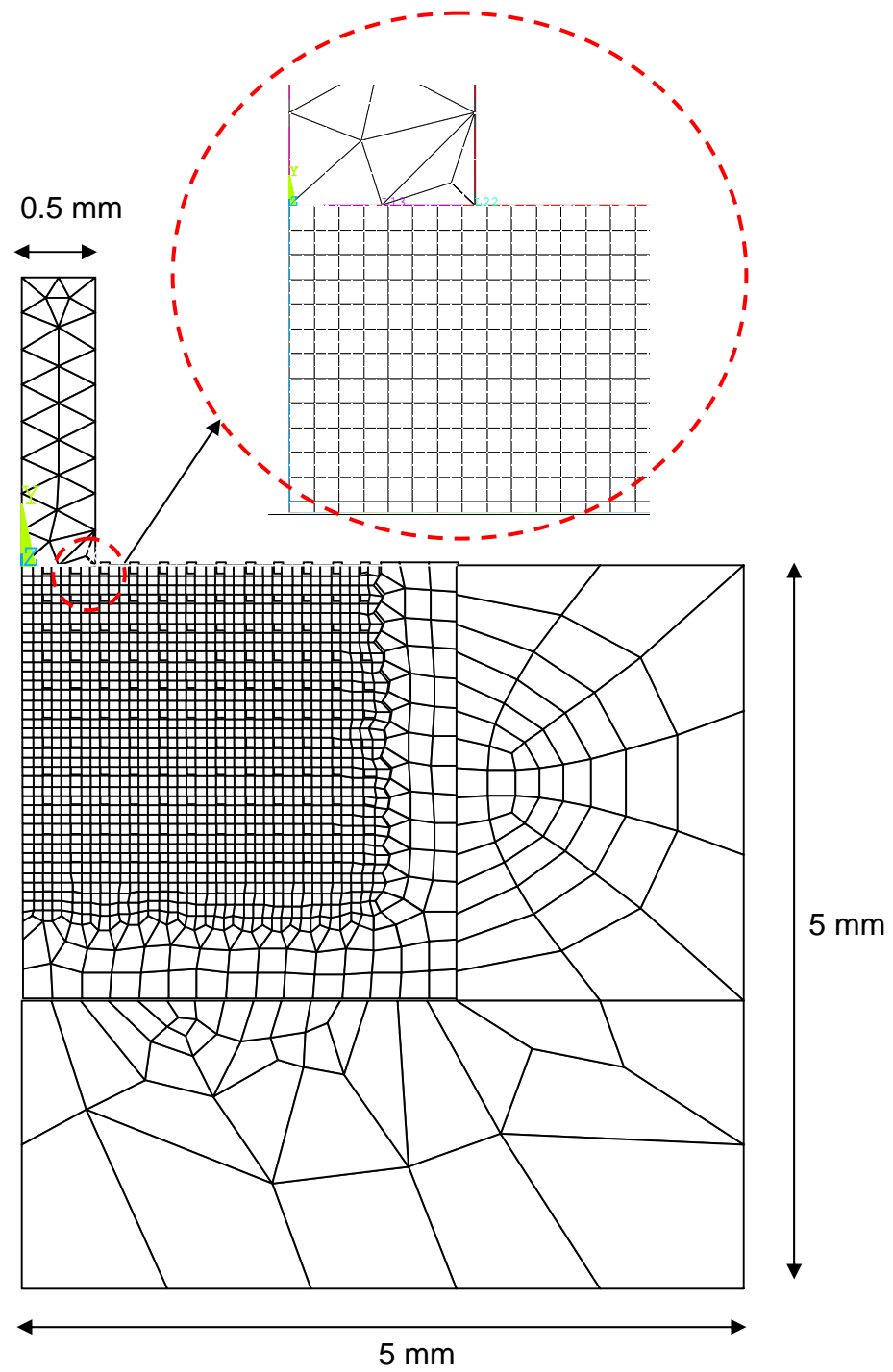


Figure 1. Finite Element Model of Impression Testing

B. MODEL INPUTS

1. Material Properties

The material properties used for the FEM simulation are listed below:

Temperature ($^{\circ}\text{K}$)	Elastic Modulus, E (GPa)	Poisson's Ratio, ν
423	24.2	0.35
373	33.5	0.35
323	42.8	0.35
298	47.5	0.35

Table 1. Elastic Properties of Sn-Ag Solder

Temperature ($^{\circ}\text{K}$)	Elastic Modulus, E (GPa)	Poisson's Ratio, ν
All	500,000	0.2

Table 2. Elastic Properties of Indenter

Temperature ($^{\circ}\text{K}$)	Proportional Limit, σ_0 (MPa)	Strain-hardening Coefficient, K (MPa)
298	30	200
373	18	184
453	10	166

Table 3. Bilinear Isotropic Properties of Sn-Ag Solder

Creep Parameters	Input Value	Units
Dorn Constant, A	7.087×10^{-8}	$\text{MPa}^{5.5}$
Activation Energy, Q	38,500	J/mol
Stress exponent, n_{crp}	5.5	-

Table 4. Creep Characteristics of Sn-Ag Solder

Temperature ($^{\circ}\text{K}$)	Proportional Limit, σ_0 (MPa)	Strain-hardening Coefficient, K (MPa)	Strain-hardening Exponent, n
298	30	25.5	0.17
323	26	23	0.17
373	18	18	0.17
423	13	13	0.17

Table 5. Multi-linear Isotropic Properties of Sn-Ag Solder

2. Multi-linear Isotropic Stress-Strain Inputs

The Multi-linear Isotropic Hardening (MISO) option in ANSYSTM uses the von Mises yield criteria coupled with an isotropic work hardening assumption. A multi-linear curve is used as an input instead of a bilinear curve as in the case for Bilinear Isotropic Hardening (BISO). The normalized strain rate $\frac{\dot{\sigma}}{\phi}$ used for both the MISO and BISO options is $5 \times 10^{-2} \text{ min}^{-1}$.

The stresses in the elastic region for the solder at each temperature are obtained from Hooke's law where

$$\sigma = \varepsilon_{el} E \quad (53)$$

until the yield point of the material at that temperature is reached. Thereafter, plasticity effects set in and plastic strains can be obtained as

$$\varepsilon_{pl} = \varepsilon_{tot} - \frac{\sigma}{E} \quad (54)$$

and the stress is given by

$$\sigma = \sigma_0 + K \varepsilon_{pl}^n \quad (47)$$

where σ is true stress, σ_0 is the proportional limit, ε_{pl} is true plastic strain, n is strain-hardening exponent and K is the strain-hardening coefficient defined as the true stress at a true strain of 1.0.

Based on these equations, the stress versus strain values were tabulated in Table 6, and the stress-strain curves for the solder at four different temperatures were plotted in Figures 2 – 5.

298K		323K		373K		423K	
Strain	Stress (MPa)	Strain	Stress (MPa)	Strain	Stress (MPa)	Strain	Stress (MPa)
0	0	0	0	0	0	0	0
0.0006315	29.996	0.0006070	25.980	0.0005370	17.990	0.0005370	12.995
0.0050047	40.004	0.0050093	35.068	0.0050097	25.117	0.0050096	18.140
0.0100086	41.457	0.0100095	36.357	0.0100096	26.116	0.0100094	18.862
0.0200047	43.000	0.0200017	37.738	0.0200017	27.192	0.0200015	19.638
0.0300073	43.967	0.0300020	38.606	0.0300019	27.870	0.0300017	20.128
0.0410456	44.753	0.0409184	39.307	0.0408482	28.414	0.0408480	20.521
0.0510590	45.324	0.0509304	39.821	0.0508602	28.817	0.0508600	20.812
0.0610702	45.806	0.0609406	40.257	0.0608704	29.157	0.0608702	21.058
0.0710800	46.226	0.0709494	40.635	0.0708792	29.454	0.0708790	21.272
0.0810887	46.598	0.0809573	40.971	0.0808871	29.716	0.0808869	21.462
0.0910966	46.934	0.0909643	41.274	0.0908941	29.953	0.0908939	21.633
0.1011037	47.240	0.1009708	41.550	0.1009006	30.169	0.1009004	21.789
0.1211164	47.783	0.1209822	42.039	0.1209120	30.553	0.1209118	22.066
0.1411275	48.255	0.1409922	42.465	0.1409220	30.886	0.1409218	22.306
0.1611372	48.674	0.1610010	42.843	0.1609308	31.182	0.1609306	22.520
0.1811461	49.052	0.1810090	43.184	0.1809388	31.448	0.1809385	22.713
0.2011541	49.396	0.2010162	43.495	0.2009460	31.691	0.2009458	22.888
0.2211615	49.713	0.2210229	43.780	0.2209527	31.915	0.2209525	23.050
0.2411684	50.007	0.2410291	44.045	0.2409589	32.122	0.2409587	23.200
0.2611748	50.281	0.2610349	44.293	0.2609647	32.316	0.2609644	23.339
0.2811808	50.538	0.2810403	44.524	0.2809701	32.497	0.2809698	23.470
0.3011865	50.780	0.3010454	44.743	0.3009752	32.668	0.3009750	23.594

Table 6. MISO Strain versus Stress Values for Sn-Ag Solder

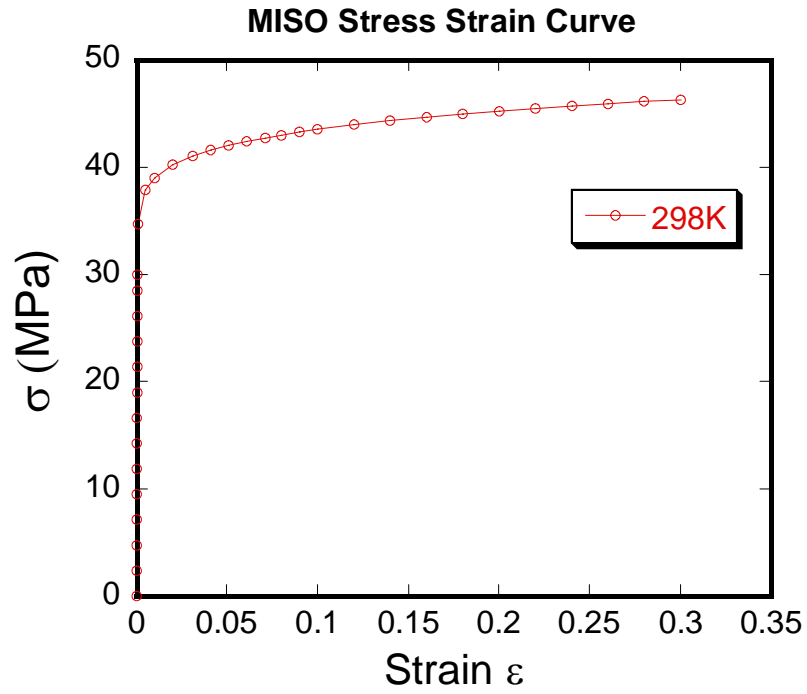


Figure 2. MISO Stress Strain Curve for Sn-Ag Solder – 298K

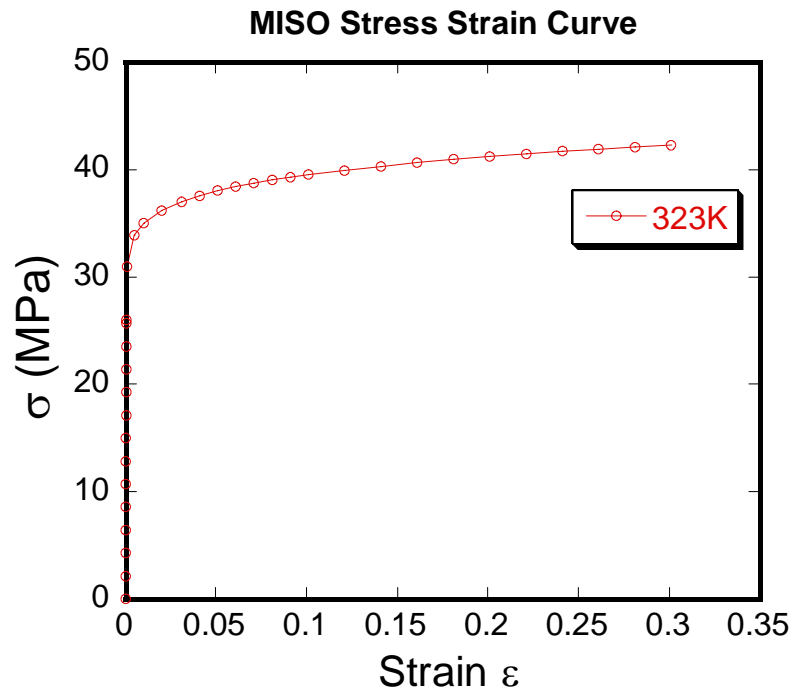


Figure 3. MISO Stress Strain Curve for Sn-Ag – 323K

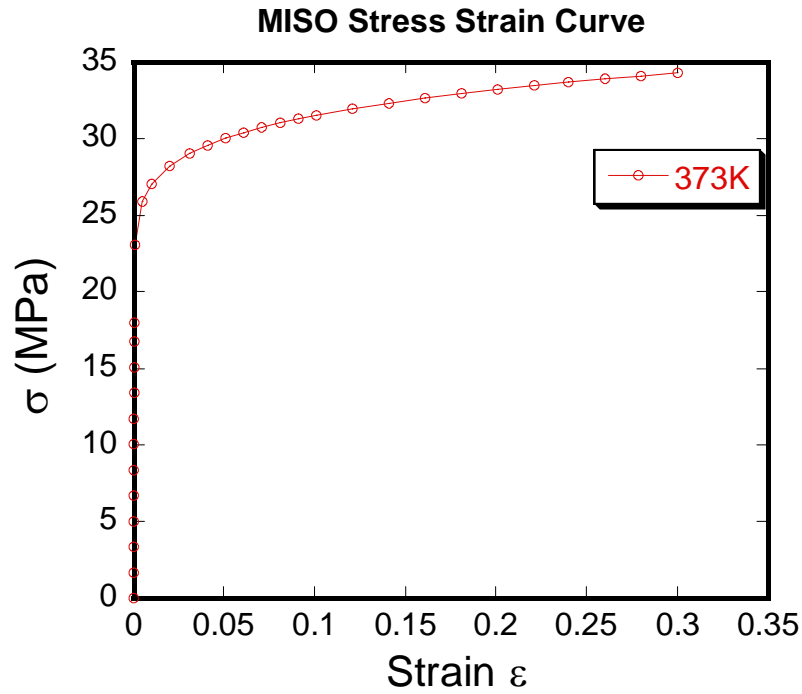


Figure 4. MISO Stress Strain Curve for Sn-Ag Solder – 373K

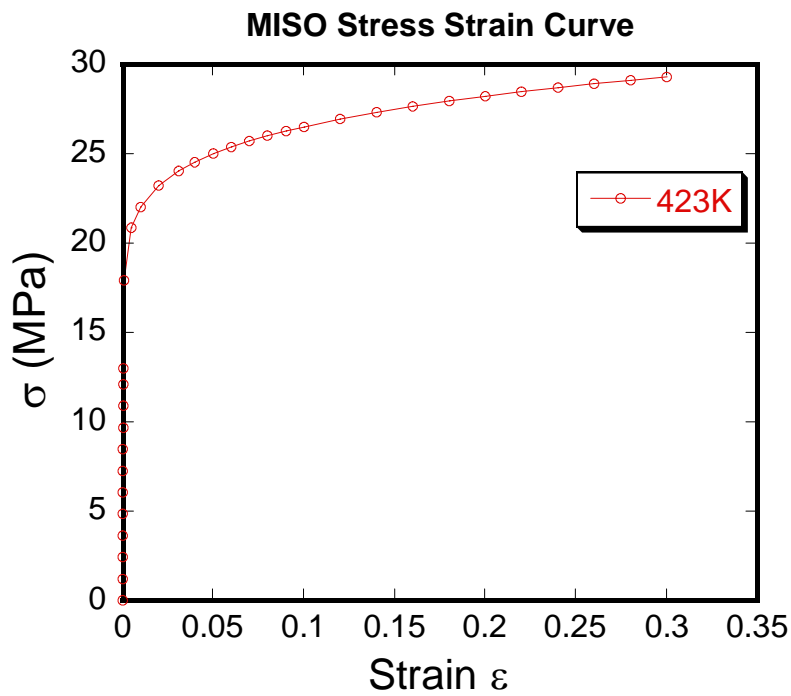


Figure 5. MISO Stress Strain Curve for Sn-Ag Solder – 423K

3. Determination of Uniaxial Yield Strength

The uniaxial yield strength is determined from the MISO input stress-strain curve at an offset of 0.1% and 0.2% strain. The plots of the determination of the uniaxial yield strength are shown in Figures 6 - 9 and the values are tabulated in Table 7:

Temperature (⁰ K)	σ_{YS} , 0.1% Strain Offset (MPa)	σ_{YS} , 0.2% Strain Offset (MPa)
298	38.00	39.05
323	33.30	34.07
373	23.65	24.32
423	17.04	17.57

Table 7. σ_{YS} from MISO input stress-strain curve at strain offsets of 0.1% and 0.2% and various temperatures

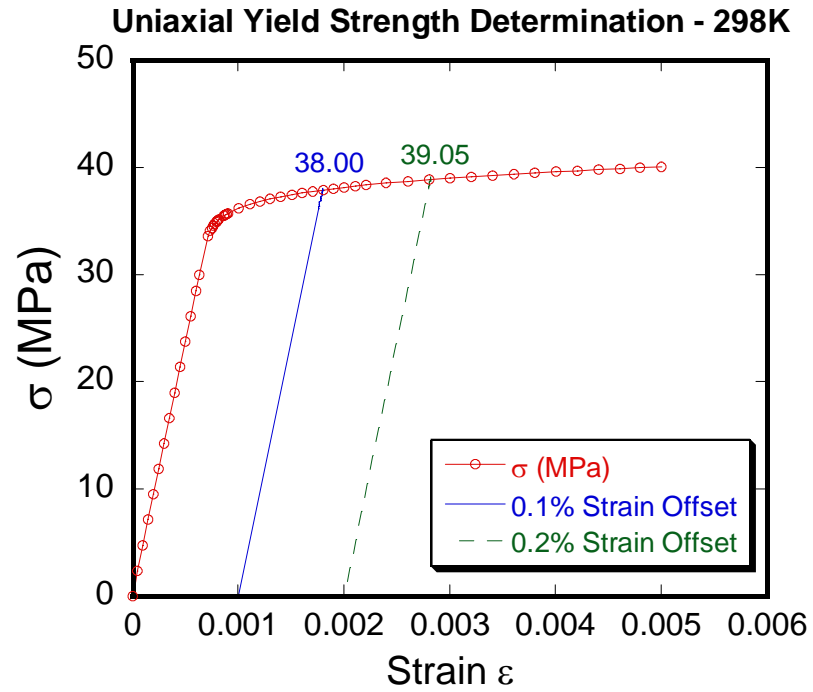


Figure 6. MISO Input Uniaxial Yield Strength Determination – 298K

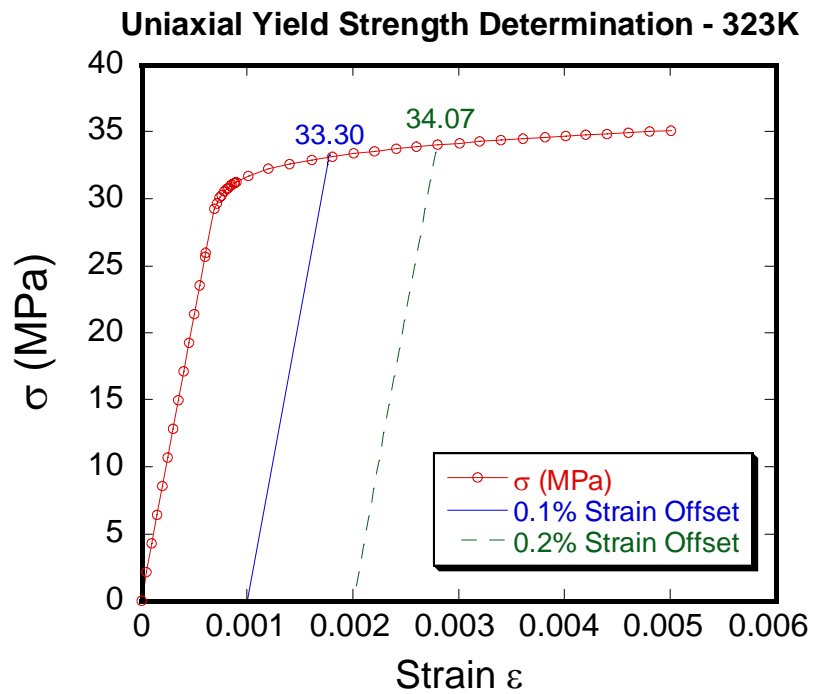


Figure 7. MISO Input Uniaxial Yield Strength Determination – 323K

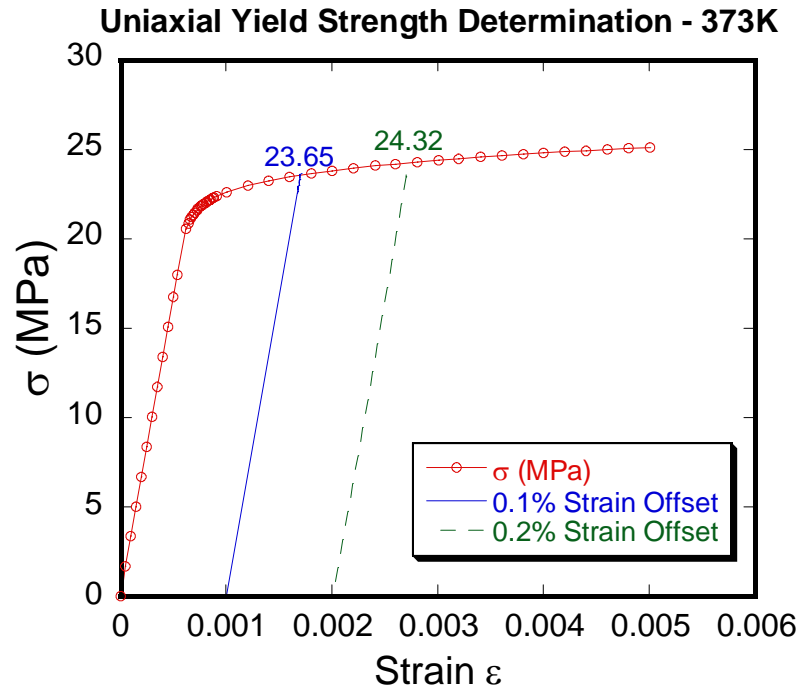


Figure 8. MISO Input Uniaxial Yield Strength Determination – 373K

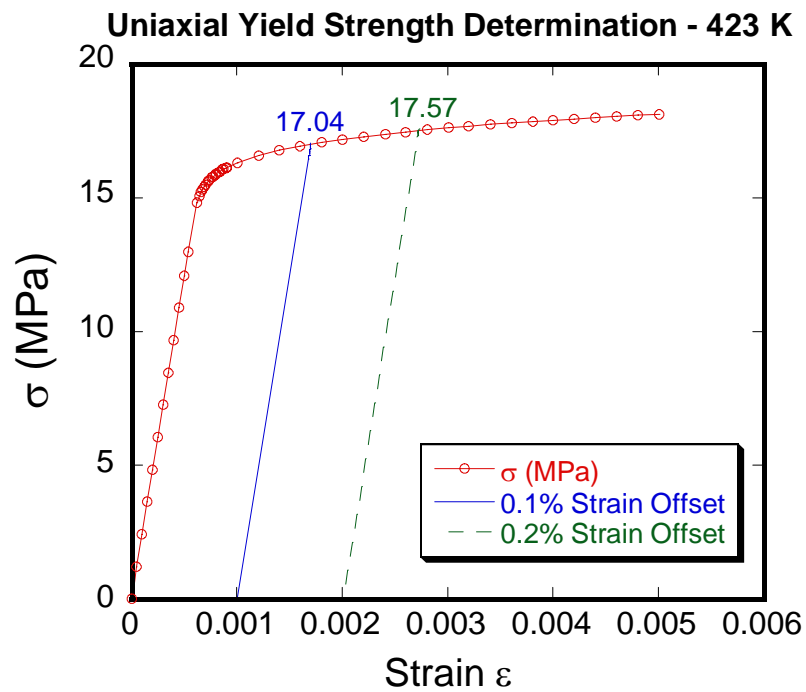


Figure 9. MISO Input Uniaxial Yield Strength Determination – 423K

4. Inputs for Investigation of Strain Rate Effects

The MISO option in ANSYS™ can be combined with the creep option to simulate the strain rate effects on the solder. Based on equation (49), it is possible to obtain a strain rate hardening law [1] given by

$$\sigma \propto C \dot{\epsilon}_{pl}^m \quad (50)$$

Correspondingly, by taking logarithm on both sides of equation (50), the impression stress and plastic strain rate can be described by the relation

$$\ln \sigma_{imp} = \ln C_{imp} + m_{imp} \ln \dot{\epsilon}_{pl,imp} \quad (51)$$

The strain-rate hardening exponent m is a parameter that is related to the creep stress exponent n_{crp} , by the relationship

$$n_{crp} = \frac{1}{m} \quad (52)$$

Therefore, the impression creep stress exponent $n_{crp,imp}$ can be similarly obtained by substituting m with m_{imp} in equation (52). The uniaxial input n_{crp} is 5.5, which gives a uniaxial m input of 0.1818. Hence, strain rates of 5e-04, 5e-05 and 5e-06 min⁻¹ are used to determine its effect on m_{imp} and hence $n_{crp,imp}$.

5. Multi-linear Stress Strain Inputs for Alternate Solder

An alternate solder was included in the analysis to ascertain whether correlation between impression and uniaxial testing is valid for a different n and K value. Hence, this alternate solder has the same elastic properties as Sn-Ag solder but different n and K values and are given in Table 8:

Temperature (°K)	Proportional Limit, σ_0 (MPa)	Strain-hardening Coefficient, K (MPa)	Strain-hardening Exponent, n
298	30	50	0.30
323	26	45	0.30
373	18	35	0.30
423	13	25	0.30

Table 8. Multi-linear Isotropic Properties of Alternate Solder

Similarly, the stress versus strain values were tabulated in Table 9, and the stress-strain curves for the solder at four different temperatures are plotted in Figures 10 - 13:

298K		323K		373K		423K	
Strain	Stress (MPa)	Strain	Stress (MPa)	Strain	Stress (MPa)	Strain	Stress (MPa)
0	0	0	0	0	0	0	0
0.0006315	29.996	0.0006070	25.980	0.0005370	17.990	0.0005370	12.995
0.0007980	33.155	0.0007738	28.839	0.0007032	20.208	0.0007024	14.577
0.0012392	35.113	0.0012150	30.602	0.0011441	21.579	0.0011428	15.556
0.0058463	40.201	0.0058220	35.181	0.0057505	25.141	0.0057480	18.101
0.0108960	42.559	0.0108716	37.303	0.0107997	26.792	0.0107967	19.280
0.0209571	45.462	0.0209326	39.916	0.0208604	28.824	0.0208567	20.731
0.0410323	49.037	0.0410078	43.133	0.0409351	31.326	0.0409305	22.518
0.0610842	51.499	0.0610596	45.349	0.0609865	33.049	0.0609814	23.749
0.0811250	53.437	0.0811003	47.093	0.0810270	34.406	0.0810214	24.718
0.1011591	55.059	0.1011344	48.553	0.1010609	35.542	0.1010549	25.530
0.1211888	56.468	0.1211641	49.821	0.1210904	36.528	0.1210841	26.234
0.1412152	57.721	0.1411904	50.949	0.1411166	37.405	0.1411099	26.860
0.1612390	58.854	0.1612142	51.969	0.1611402	38.198	0.1611333	27.427
0.1812609	59.892	0.1812360	52.903	0.1811619	38.924	0.1811548	27.946
0.2012811	60.852	0.2012562	53.767	0.2011820	39.596	0.2011746	28.426
0.2212999	61.747	0.2212750	54.572	0.2212007	40.223	0.2211931	28.873
0.2413176	62.586	0.2412927	55.328	0.2412182	40.810	0.2412105	29.293
0.2613343	63.378	0.2613094	56.040	0.2612348	41.365	0.2612268	29.689
0.2813501	64.129	0.2813251	56.716	0.2812504	41.890	0.2812423	30.064
0.3013651	64.842	0.3013401	57.358	0.3012654	42.390	0.3012571	30.421

Table 9. MISO Strain versus Stress Values for Alternate Solder

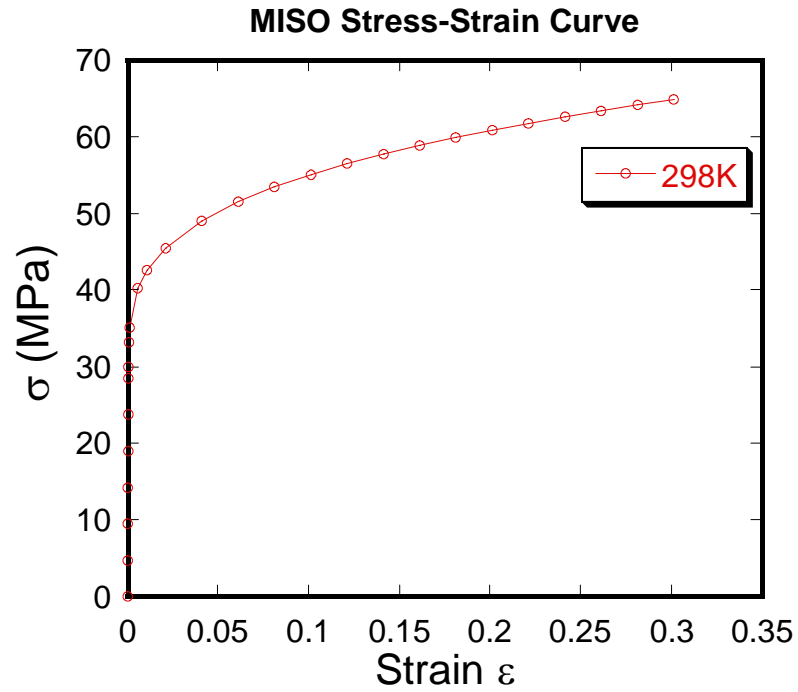


Figure 10. MISO Stress Strain Curve for Alternate Solder – 298K

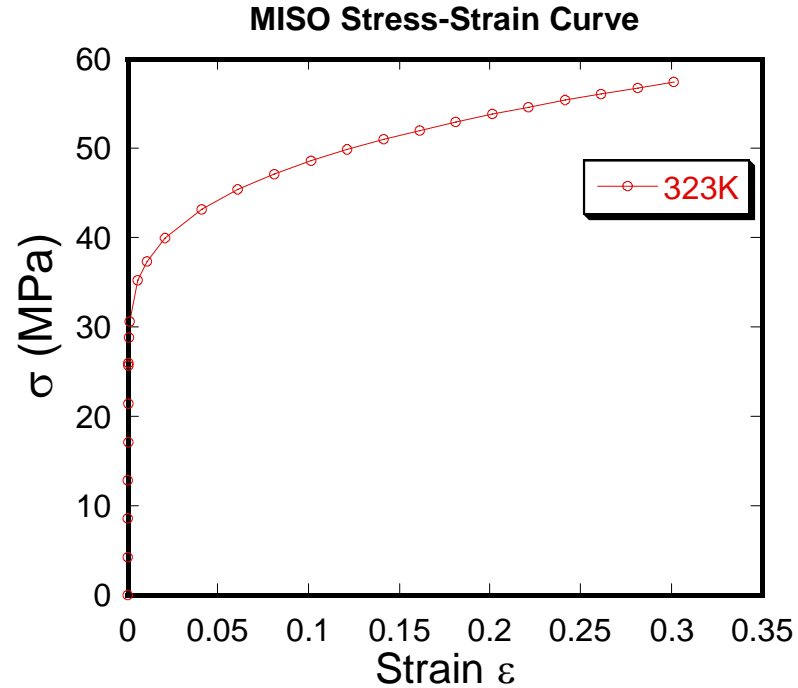


Figure 11. MISO Stress Strain Curve for Alternate Solder – 323K

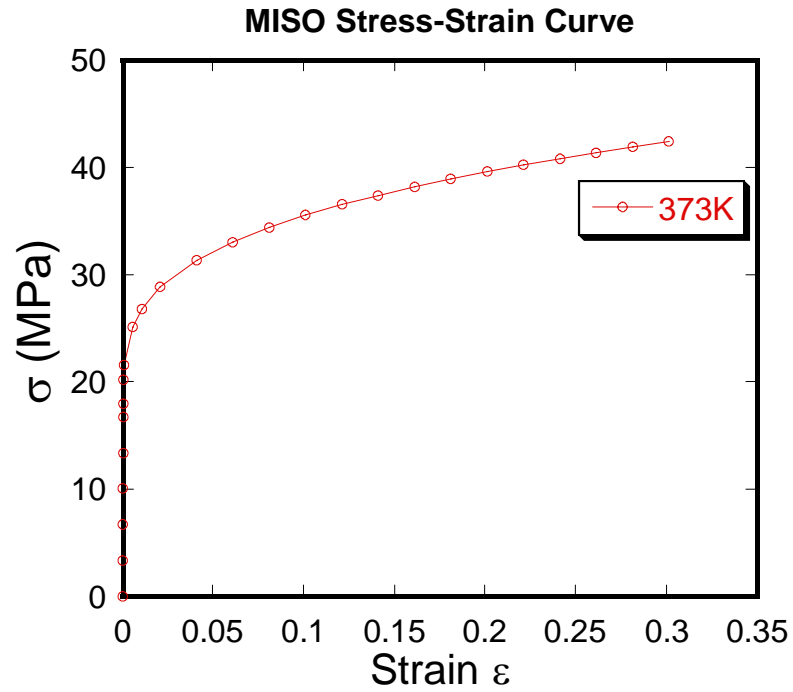


Figure 12. MISO Stress Strain Curve for Alternate Solder – 373K

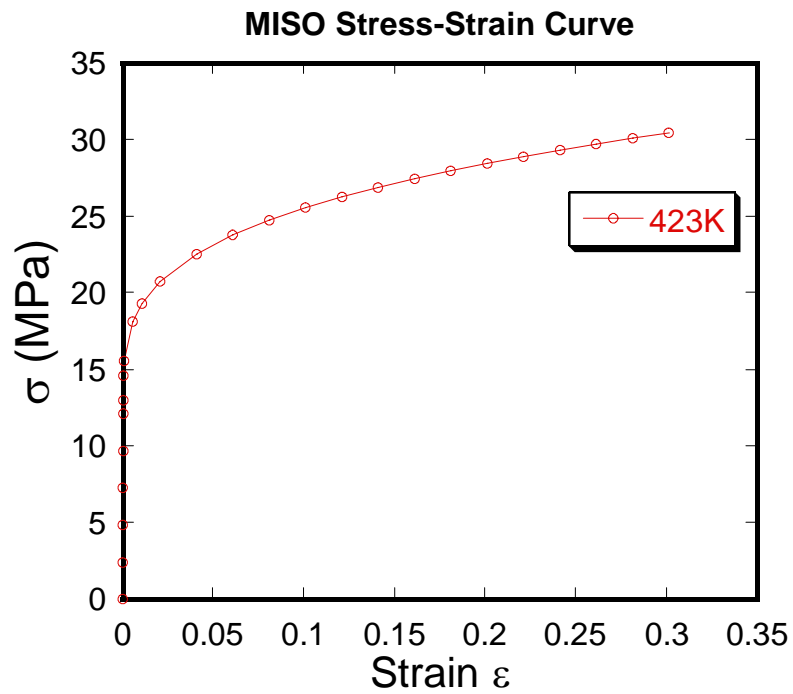


Figure 13. MISO Stress Strain Curve for Alternate Solder – 423K

THIS PAGE INTENTIONALLY LEFT BLANK

IV. RESULTS

A. BILINEAR ISOTROPIC ANALYSIS FOR Sn-Ag SOLDER

1. Impression Stress-Strain Plots for BISO Analysis

The impression stress-strain plots using BISO option are shown below:

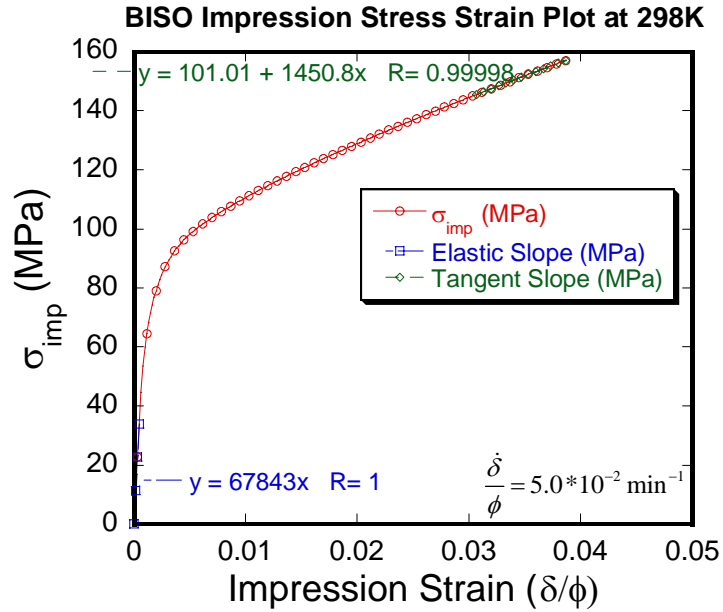


Figure 14. BISO Impression Stress-Strain Plot for Sn-Ag Solder – 298K

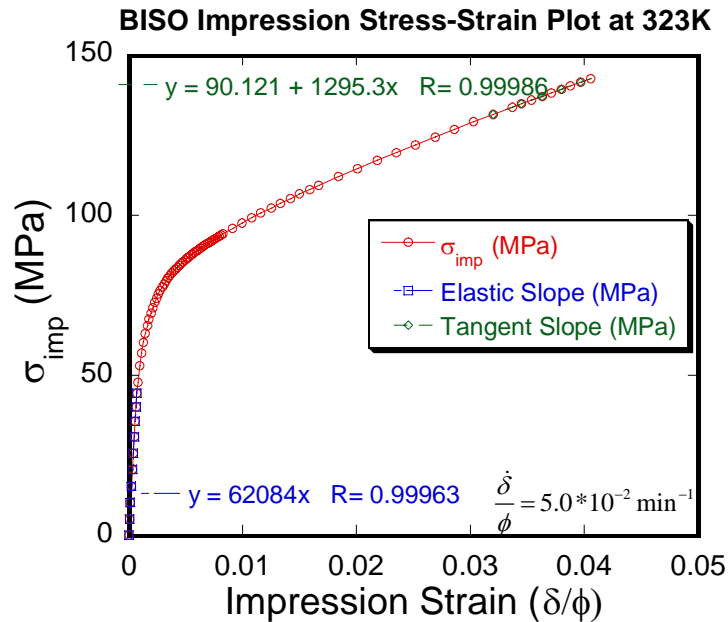


Figure 15. BISO Impression Stress-Strain Plot for Sn-Ag Solder – 323K

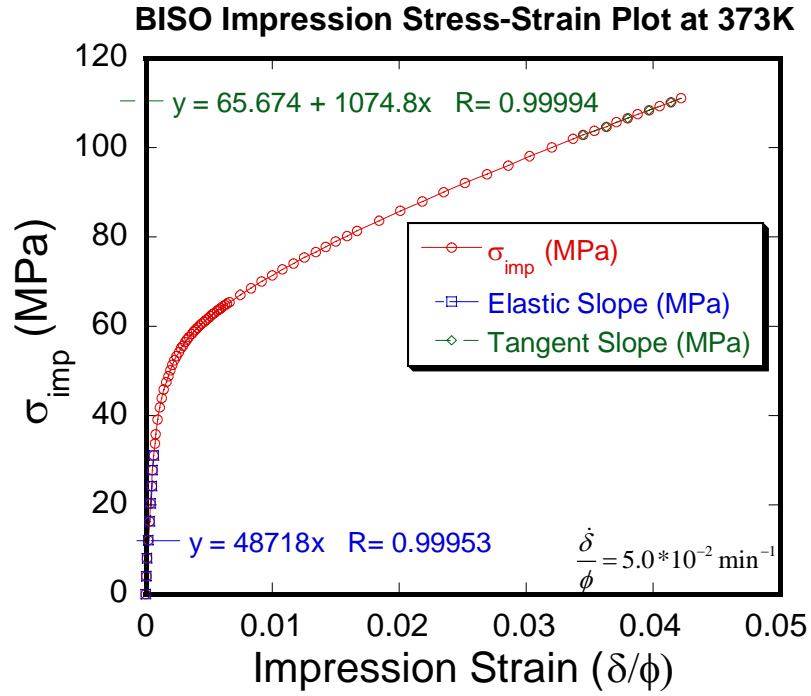


Figure 16. BISO Impression Stress-Strain Plot for Sn-Ag Solder – 373K

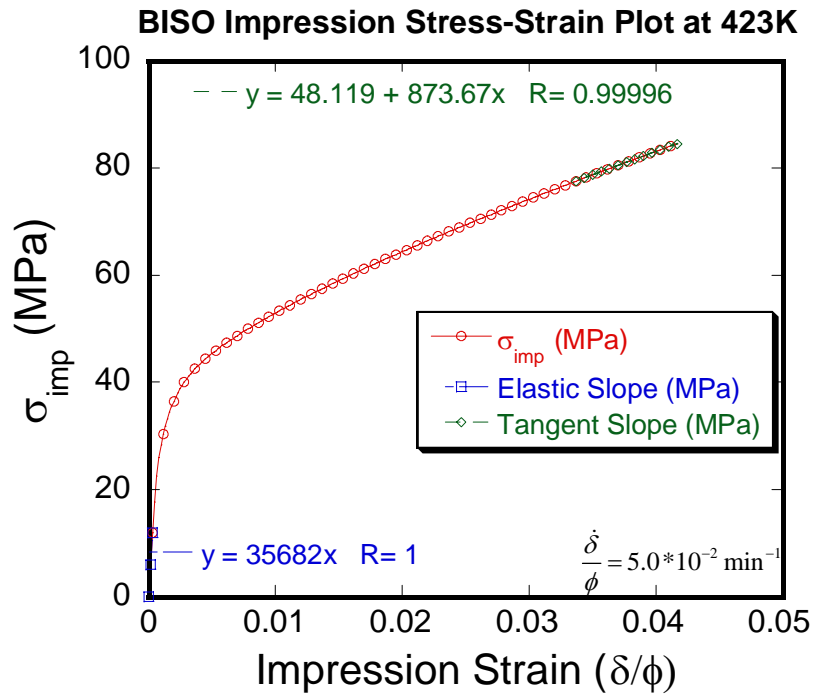


Figure 17. BISO Impression Stress-Strain Plot for Sn-Ag Solder – 423K

2. Determination of Impression Elastic Modulus E_{imp}^{BISO} for BISO Analysis

The impression elastic modulus using the BISO option E_{imp}^{BISO} is determined from the elastic slope of the impression stress-strain curves up to the proportional limit and is given in the units of MPa. These are shown and plotted from Figures 14 – 17.

Hence, E_{imp}^{BISO} for the four different simulated conditions using the BISO option for the Sn-Ag solder are tabulated in Table 10:

Temperature ($^{\circ}\text{K}$)	E_{imp}^{BISO} (MPa)
298	67843
323	62084
373	48718
423	35682

Table 10. E_{imp}^{BISO} from BISO Analysis for Sn-Ag Solder at Various Temperatures

3. Determination of Impression Strain Hardening Coefficient K_{imp}^{BISO} for BISO Analysis

The impression strain-hardening coefficient for BISO analysis K_{imp}^{BISO} is determined from the tangent slope of the impression stress-strain curve up to a strain value where reasonable plastic deformation has set in and solution convergence has reached its limits. K_{imp}^{BISO} is also given in the units of MPa. These are also shown and plotted from Figures 14 – 17.

Hence, K_{imp}^{BISO} for the four different simulated conditions using the BISO option for the Sn-Ag solder are tabulated in Table 11:

Temperature ($^{\circ}\text{K}$)	K_{imp}^{BISO} (MPa)
298	1450.8
323	1295.3
373	1074.8
423	873.7

Table 11. K_{imp}^{BISO} from BISO Analysis for Sn-Ag Solder at Various Temperatures

B. MULTILINEAR ISOTROPIC ANALYSIS FOR Sn-Ag SOLDER

1. Impression Stress-Strain Plots for MISO Analysis

The impression stress-strain values and plots using the MISO option for the Sn-Ag Solder are shown below:

298K		323K		373K		423K	
Strain	Stress (MPa)	Strain	Stress (MPa)	Strain	Stress (MPa)	Strain	Stress (MPa)
0	0	0	0	0	0	0	0
1.667E-04	11.310	1.667E-04	10.262	1.667E-04	8.131	1.667E-04	5.950
3.333E-04	22.620	3.333E-04	20.524	3.333E-04	16.262	3.333E-04	11.901
5.000E-04	33.922	5.000E-04	30.771	5.000E-04	24.321	5.000E-04	17.775
6.667E-04	45.013	6.667E-04	40.738	6.667E-04	31.872	6.667E-04	23.231
8.333E-04	55.181	8.333E-04	49.706	8.333E-04	38.092	8.333E-04	27.700
1.000E-03	63.515	1.000E-03	56.907	1.000E-03	43.017	1.000E-03	31.244
1.167E-03	70.213	1.167E-03	62.766	1.167E-03	47.008	1.167E-03	34.111
1.333E-03	75.598	1.333E-03	67.446	1.333E-03	50.191	1.333E-03	36.388
1.500E-03	80.055	1.500E-03	71.329	1.500E-03	52.878	1.500E-03	38.320
1.667E-03	83.941	1.667E-03	74.703	1.667E-03	55.213	1.667E-03	39.998
2.000E-03	90.442	2.000E-03	80.362	2.000E-03	59.152	2.000E-03	42.827
2.333E-03	95.770	2.333E-03	84.980	2.333E-03	62.373	2.333E-03	45.143
2.667E-03	100.270	2.667E-03	88.875	2.667E-03	65.076	2.667E-03	47.085
3.000E-03	104.110	3.000E-03	92.200	3.000E-03	67.384	3.000E-03	48.744
3.333E-03	107.460	3.333E-03	95.088	3.333E-03	69.380	3.333E-03	50.179
3.667E-03	110.390	3.667E-03	97.611	3.667E-03	71.119	3.667E-03	51.429
4.000E-03	112.970	4.000E-03	99.830	4.000E-03	72.639	4.000E-03	52.520
4.333E-03	115.230	4.333E-03	101.770	4.333E-03	73.968	4.333E-03	53.475
4.667E-03	117.230	4.667E-03	103.490	4.667E-03	75.150	4.667E-03	54.326
5.000E-03	119.030	5.000E-03	105.030	5.000E-03	76.218	5.000E-03	55.094
6.666E-03	125.639	6.666E-03	110.689	6.666E-03	80.132	6.666E-03	57.911
8.333E-03	130.312	8.333E-03	114.707	8.333E-03	82.957	8.333E-03	59.946
9.999E-03	133.813	9.999E-03	117.738	9.999E-03	85.119	9.999E-03	61.503
1.167E-02	136.615	1.167E-02	120.174	1.167E-02	86.882	1.167E-02	62.775
1.333E-02	139.046	1.333E-02	122.298	1.333E-02	88.433	1.333E-02	63.894
1.500E-02	141.191	1.500E-02	124.175	1.500E-02	89.802	1.500E-02	64.882
1.667E-02	143.105	1.667E-02	125.856	1.667E-02	91.036	1.667E-02	65.774
1.833E-02	144.876	1.833E-02	127.411	1.833E-02	92.177	1.833E-02	66.597
2.000E-02	146.521	2.000E-02	128.858	2.000E-02	93.239	2.000E-02	67.364
2.167E-02	148.089	2.167E-02	130.239	2.167E-02	94.252	2.167E-02	68.097
2.333E-02	149.601	2.333E-02	131.572	2.333E-02	95.231	2.333E-02	68.805
2.500E-02	151.079	2.500E-02	132.875	2.500E-02	96.188	2.500E-02	69.497
2.666E-02	152.529	2.666E-02	134.154	2.666E-02	97.125	2.666E-02	70.174
2.833E-02	153.960	2.833E-02	135.416	2.833E-02	98.048	2.833E-02	70.842

Table 12. MISO Impression Stress vs Strain Values for Sn-Ag Solder

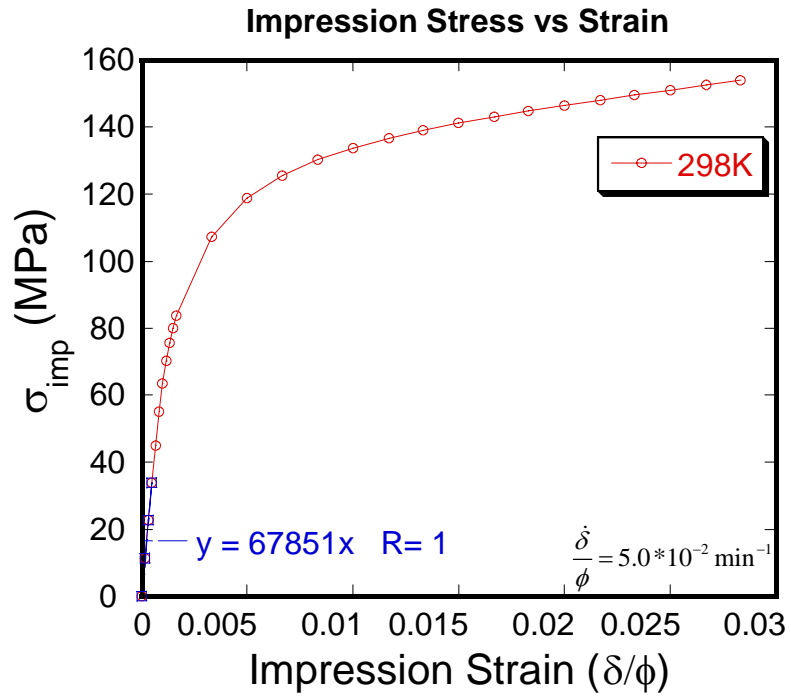


Figure 18. MISO Impression Stress-Strain Plot for Sn-Ag Solder – 298K

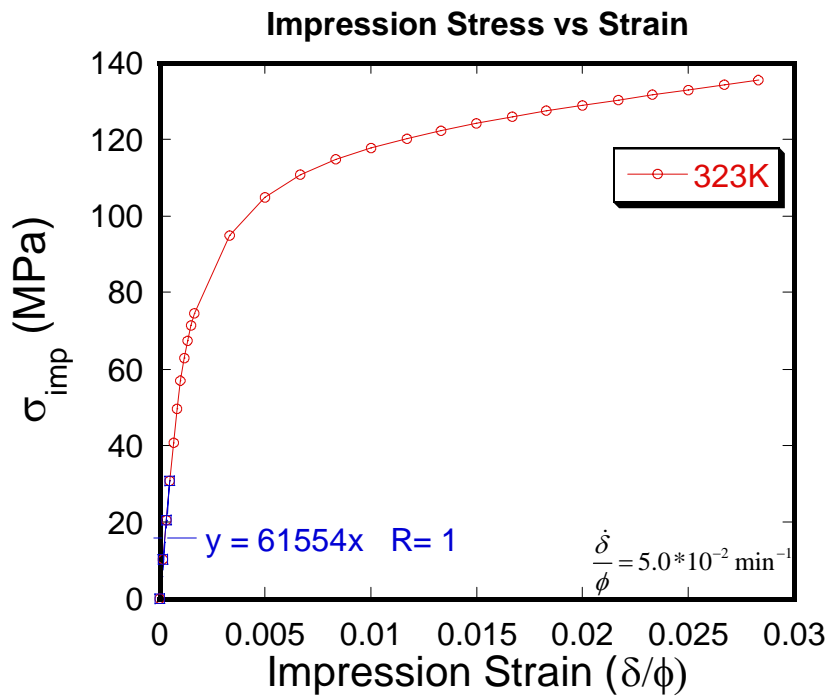


Figure 19. MISO Impression Stress-Strain Plot for Sn-Ag Solder – 323K

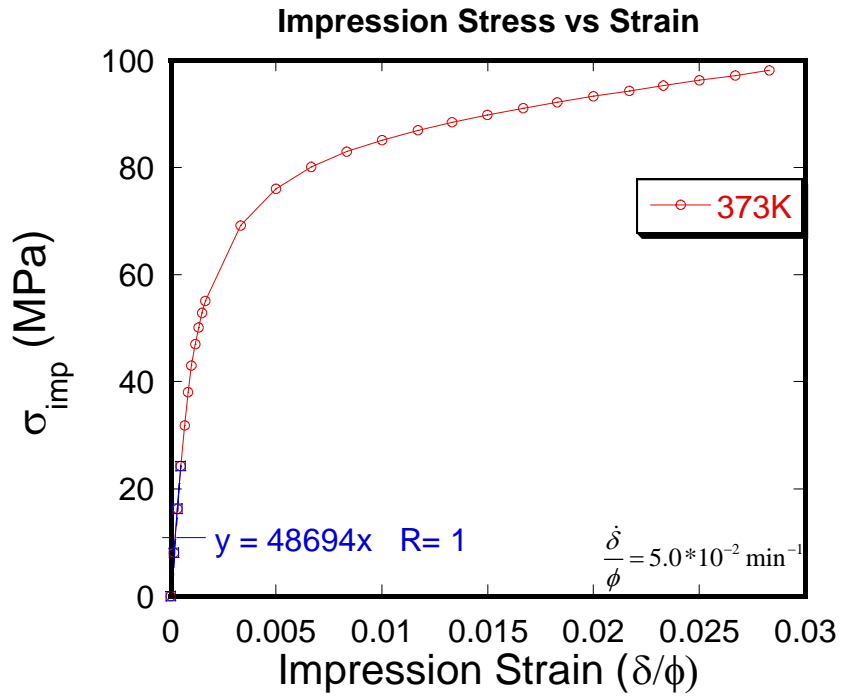


Figure 20. MISO Impression Stress-Strain Plot for Sn-Ag Solder – 373K

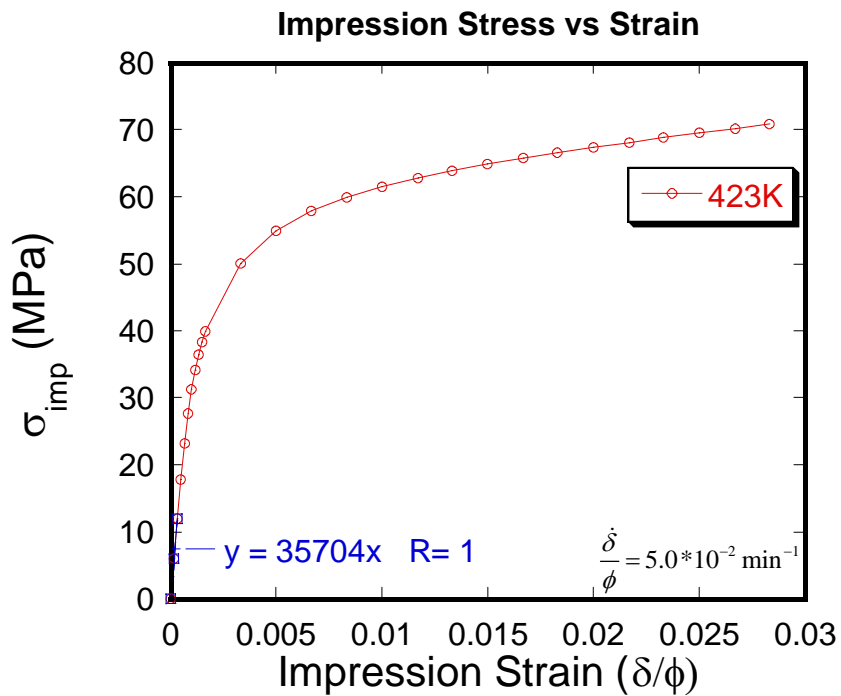


Figure 21. MISO Impression Stress-Strain Plot for Sn-Ag Solder – 423K

2. Determination of Impression Elastic Modulus E_{imp}^{MISO} for MISO Analysis

The impression elastic modulus E_{imp}^{MISO} is determined from the elastic slope of the impression stress-strain curve up to the proportional limit and is given in the units of MPa. These are shown and plotted from Figures 18 – 21. Since the elastic constants used for both the MISO and BISO options are similar, both of their corresponding impression elastic modulus should be approximately equivalent.

Hence, E_{imp}^{MISO} for the four different simulated conditions using the MISO option for the Sn-Ag solder are tabulated in Table 13:

Temperature ($^{\circ}\text{K}$)	E_{imp}^{MISO} (MPa)
298	67851
323	61554
373	48694
423	35704

Table 13. E_{imp}^{MISO} from MISO Analysis for Sn-Ag Solder at Various Temperatures

3. Determination of Impression Yield Strength for MISO Analysis

The impression yield strength is determined from the impression stress-strain plots at an offset of 0.1% and 0.2% strain. The plots of the determination of the impression yield strength are shown from Figures 22 - 25 and the values are tabulated in Table 14:

Temperature ($^{\circ}\text{K}$)	$\sigma_{YS,imp, 0.1\% \text{ Strain Offset}}$ (MPa)	$\sigma_{YS,imp, 0.2\% \text{ Strain Offset}}$ (MPa)
298	97.70	109.90
323	86.17	97.25
373	62.33	70.12
423	44.99	50.70

Table 14. $\sigma_{YS,imp}$ from MISO Analysis for Sn-Ag Solder at Various Temperatures

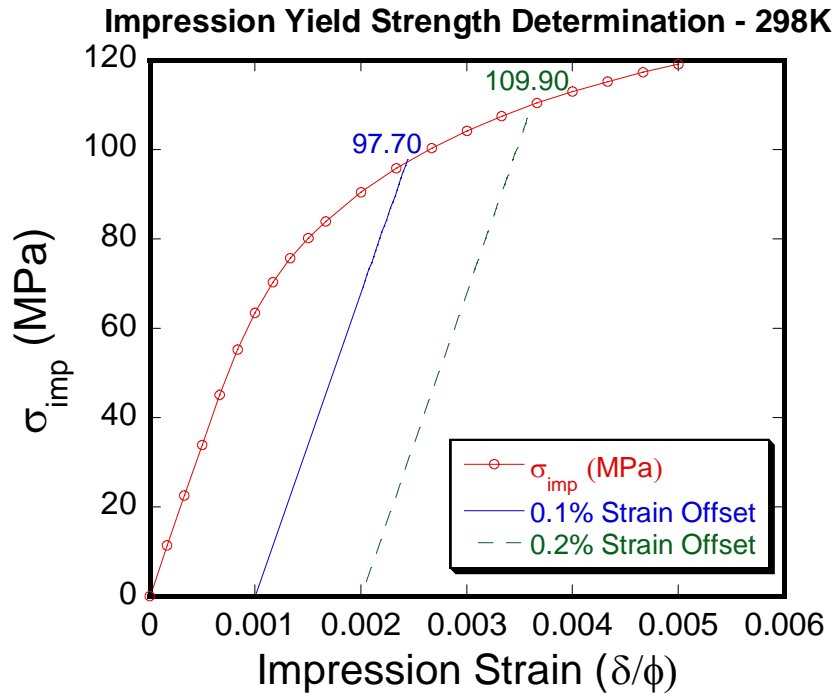


Figure 22. MISO Impression Yield Strength Determination for Sn-Ag Solder at 298K

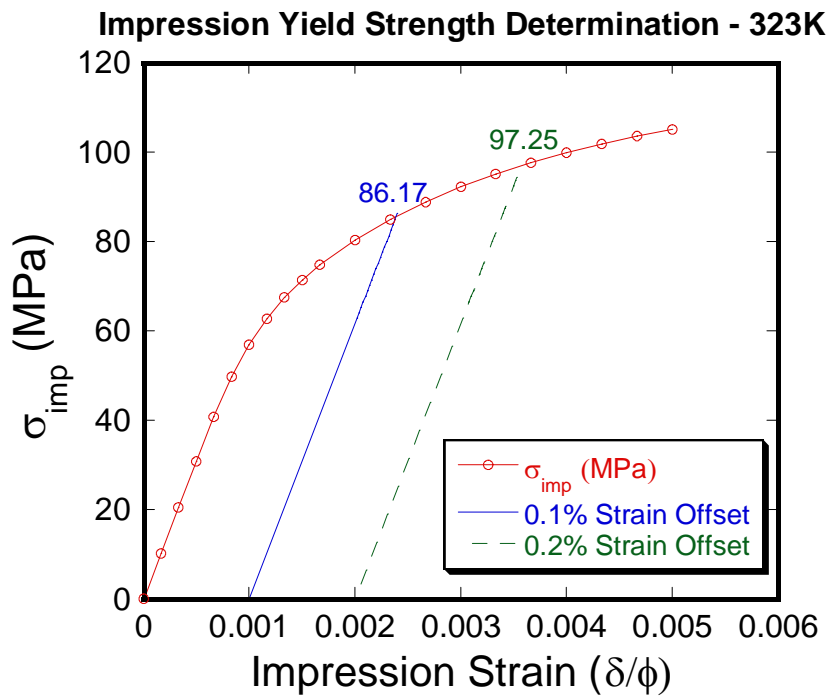


Figure 23. MISO Impression Yield Strength Determination for Sn-Ag Solder at 323K

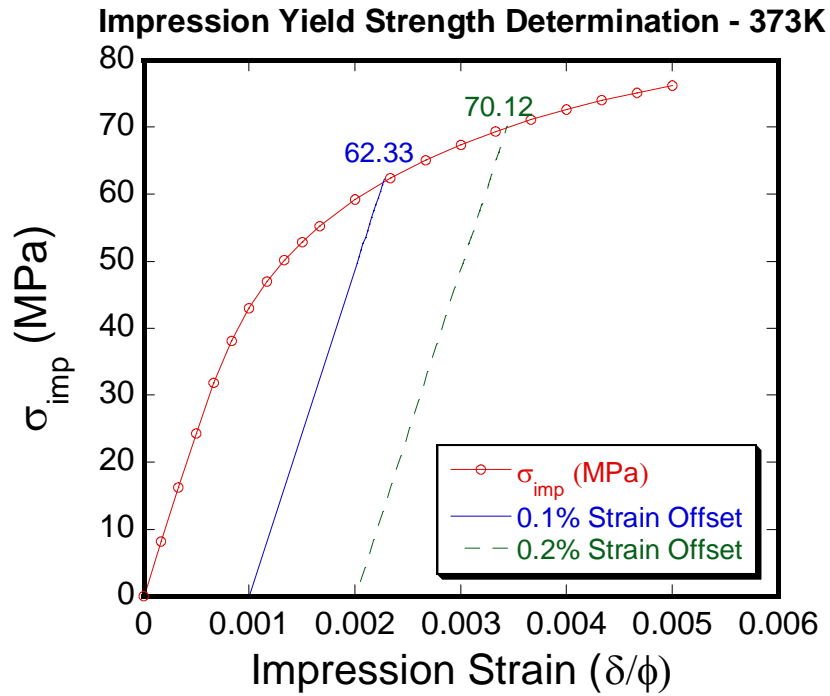


Figure 24. MISO Impression Yield Strength Determination for Sn-Ag Solder at 373K

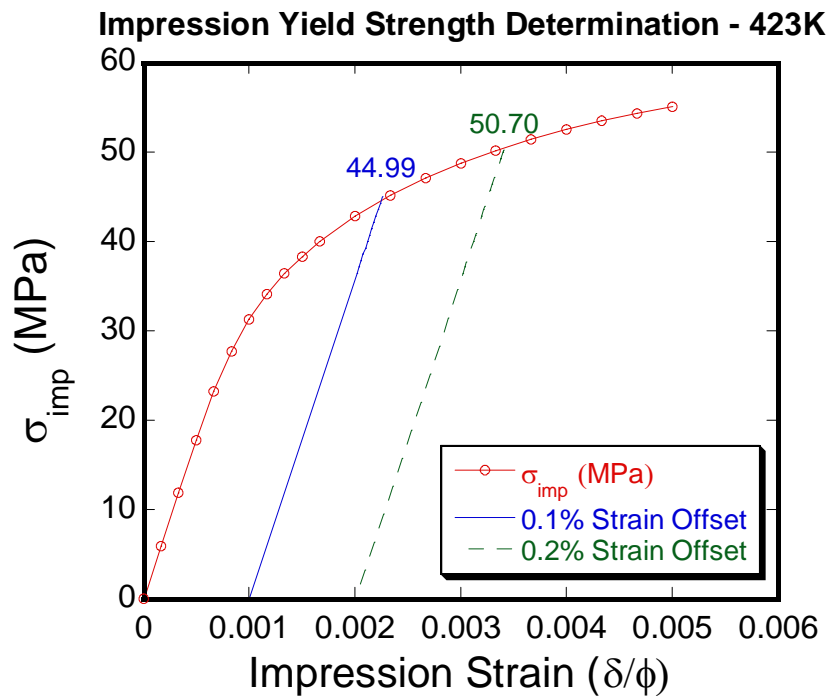


Figure 25. MISO Impression Yield Strength Determination for Sn-Ag Solder at 423K

4. Determination of n_{imp} and K_{imp}^{MISO} Values for MISO Analysis

As mentioned in the methodology, the stress-strain relationship characterizing the strain hardening of a material is given by

$$\sigma = \sigma_0 + K \varepsilon_{pl}^n \quad (47)$$

Taking the logarithm on both sides of the above equation, the impression stress and strains can be described by the relationship

$$\ln(\sigma_{imp} - \sigma_{0,imp}) = n_{imp} \ln \varepsilon_{pl,imp} + \ln K_{imp} \quad (48)$$

Hence, the slope of the graph is the impression strain hardening exponent n_{imp} and the intercept is $\ln K_{imp}$. $\sigma_{0,imp}$ is the impression proportional limit and can be determined from the impression stress-strain curve as the point where plastic strains first set in. Similarly, the curves are plotted up to a strain value where reasonable plastic deformation has set in and solution convergence has reached its limits.

The plots for the determination $\sigma_{0,imp}$ are shown from Figures 26 – 29, and the plots of $\ln(\sigma_{imp} - \sigma_{0,imp})$ vs $\ln \varepsilon_{pl,imp}$ from the impression test simulation at various temperatures are shown from Figures 30 – 33. The values of $\sigma_{0,imp}$, n_{imp} and K_{imp}^{MISO} are tabulated in Table 15:

Temperature ($^{\circ}\text{K}$)	$\sigma_{0,imp}$ (MPa)	$\ln K_{imp}^{MISO}$	K_{imp}^{MISO} (MPa)	n_{imp}
298	48.0	5.2998	200.3	0.1759
323	42.0	5.1694	175.8	0.1750
373	27.0	4.8957	133.7	0.1748
423	20.0	4.5607	95.65	0.1749

Table 15. $\sigma_{0,imp}$, n_{imp} & K_{imp}^{MISO} from MISO Analysis for Sn-Ag Solder at Various Temperatures

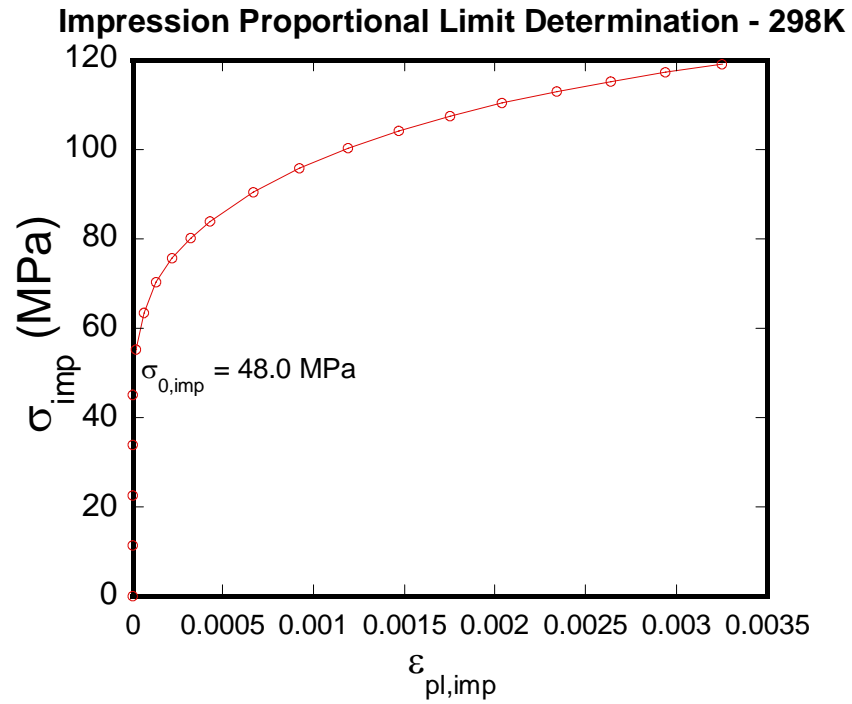


Figure 26. Determination of $\sigma_{0,imp}$ at 298K

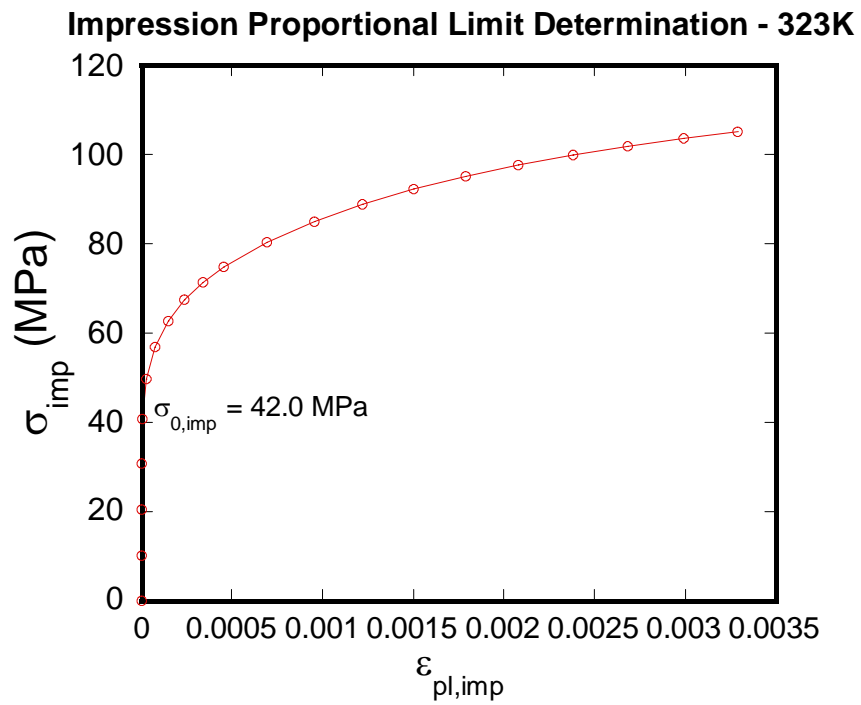


Figure 27. Determination of $\sigma_{0,imp}$ at 323K

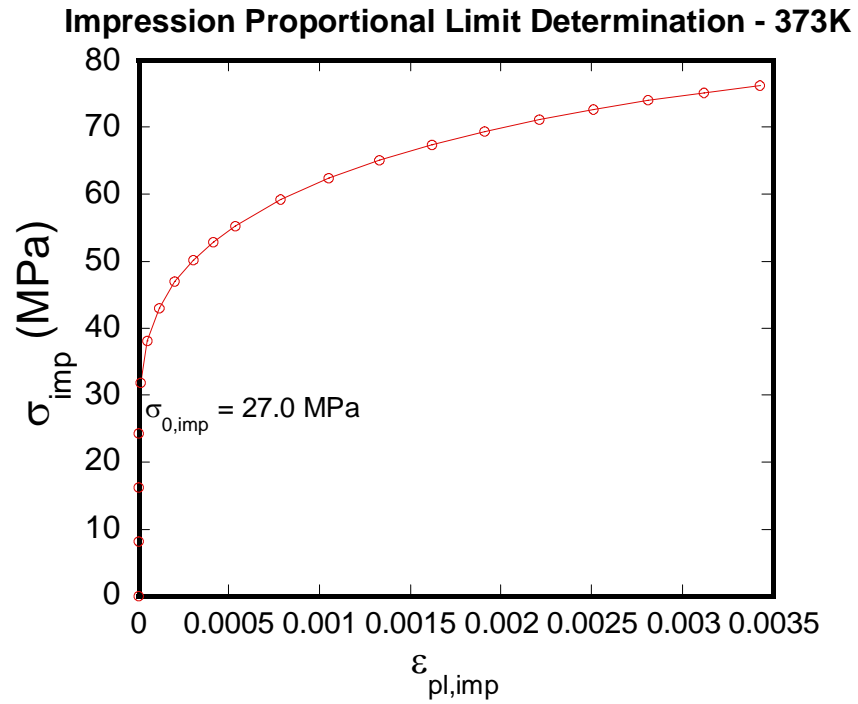


Figure 28. Determination of $\sigma_{0,imp}$ at 373K

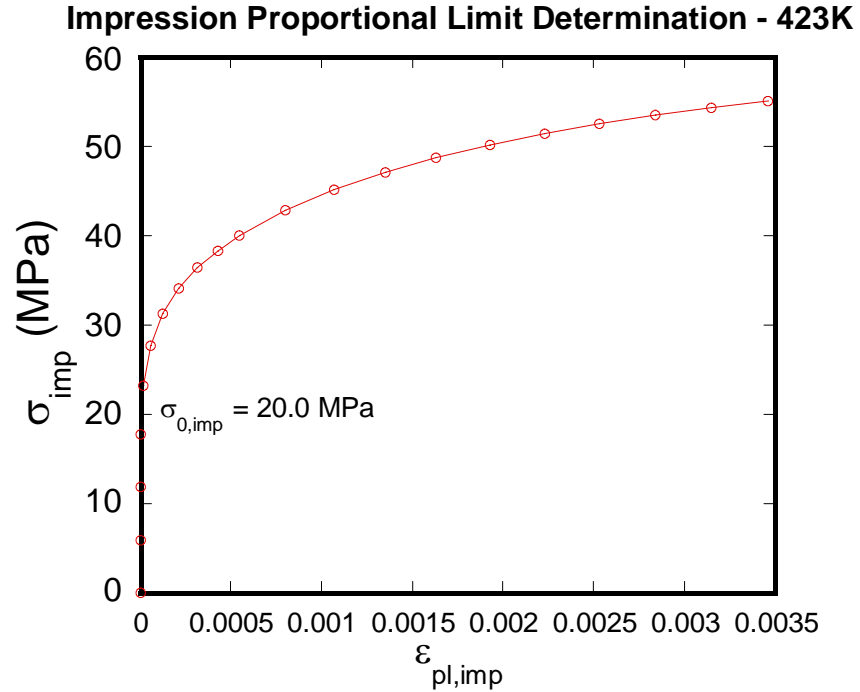


Figure 29. Determination of $\sigma_{0,imp}$ at 423K

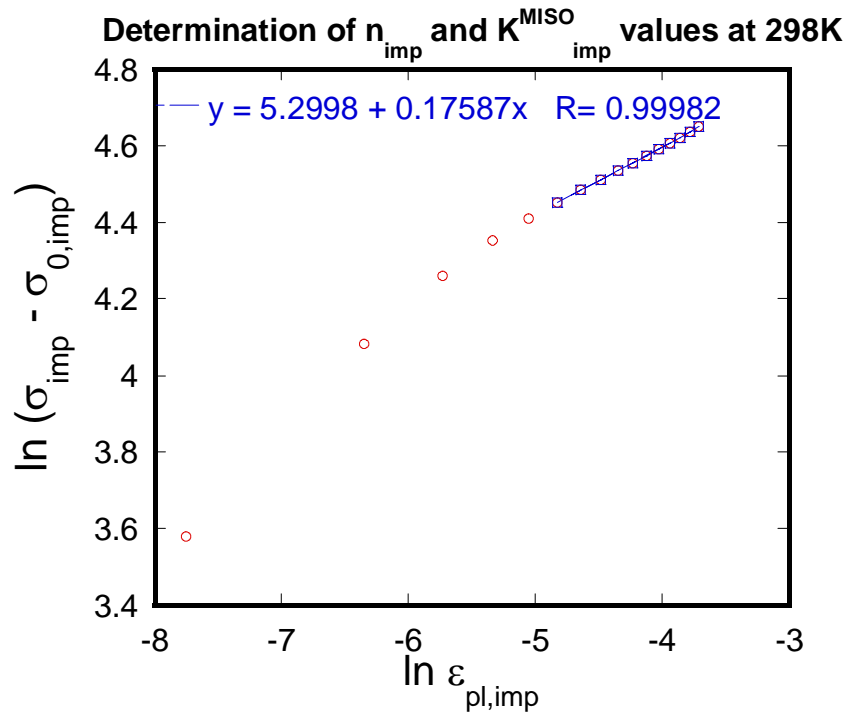


Figure 30. Plot of $\ln(\sigma_{imp} - \sigma_{0,imp})$ vs $\ln \varepsilon_{pl,imp}$ for Sn-Ag Solder at 298K

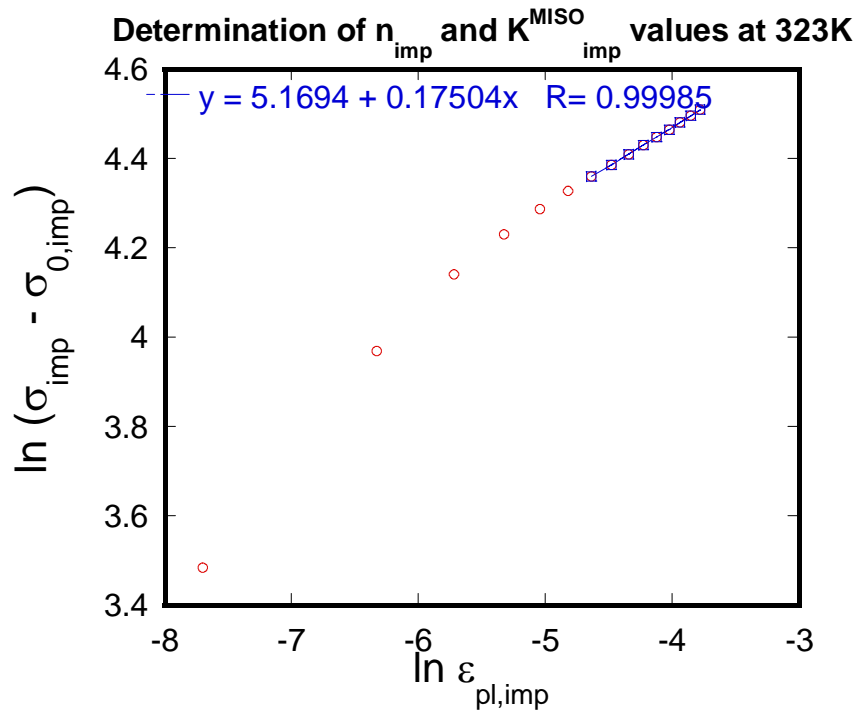


Figure 31. Plot of $\ln(\sigma_{imp} - \sigma_{0,imp})$ vs $\ln \varepsilon_{pl,imp}$ for Sn-Ag Solder at 323K

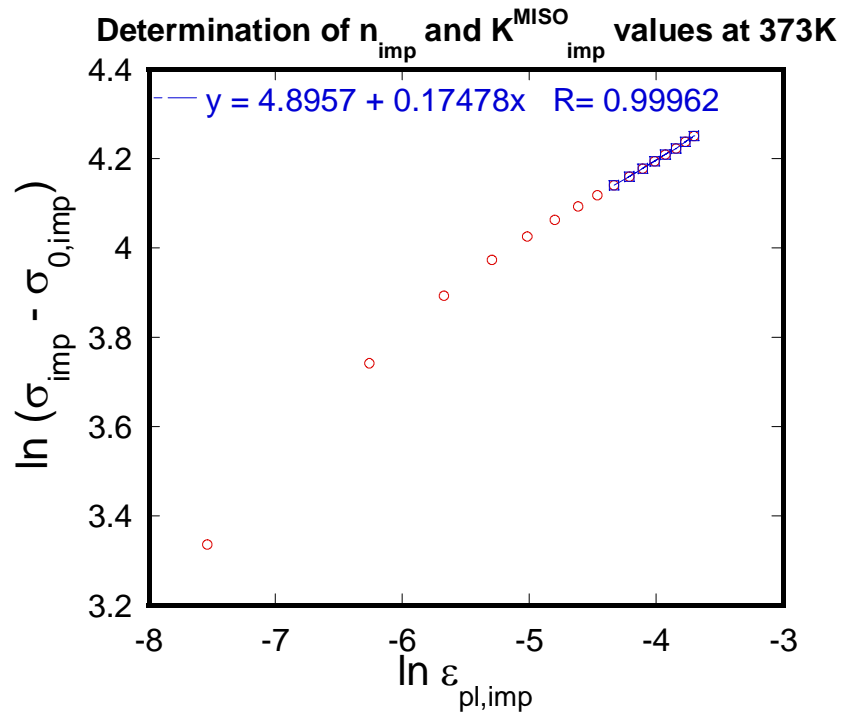


Figure 32. Plot of $\ln(\sigma_{imp} - \sigma_{0,imp})$ vs $\ln \varepsilon_{pl,imp}$ for Sn-Ag Solder at 373K

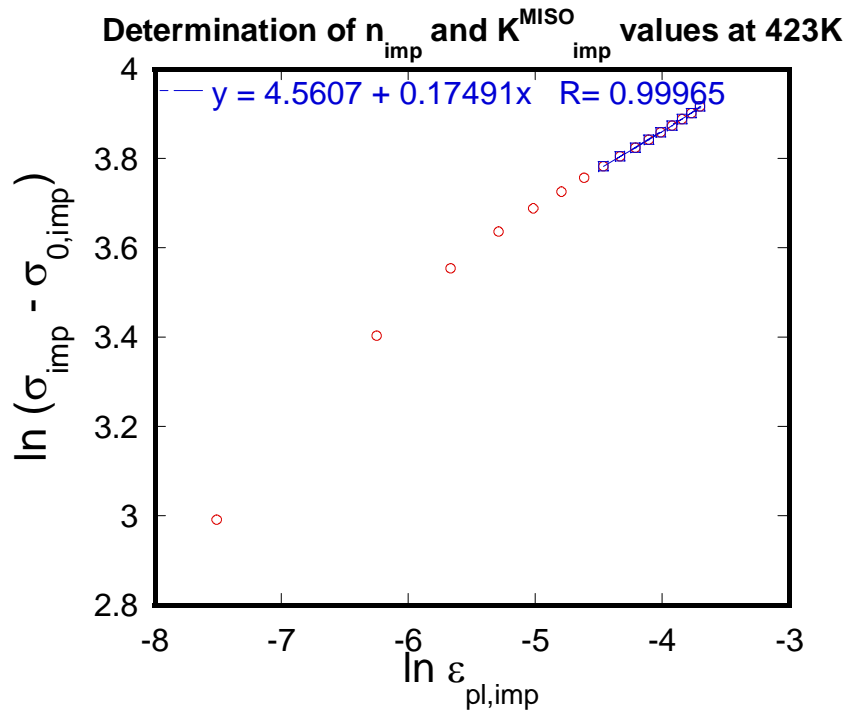


Figure 33. Plot of $\ln(\sigma_{imp} - \sigma_{0,imp})$ vs $\ln \varepsilon_{pl,imp}$ for Sn-Ag Solder at 423K

5. Determination of m_{imp} and $n_{crp,imp}$ Values for MISO Analysis of Sn-Ag Solder

Based on equation (49), it is possible to obtain a strain rate hardening law [1] given by

$$\sigma \propto C \dot{\epsilon}_{pl}^m \quad (50)$$

where C is the strain-rate hardening coefficient and m is the strain-rate hardening exponent. Correspondingly, by taking logarithm on both sides of equation (50), the impression stress and plastic strain rate can be described by the relation

$$\ln \sigma_{imp} = \ln C_{imp} + m_{imp} \ln \dot{\epsilon}_{pl,imp} \quad (51)$$

where m_{imp} is the impression strain-rate hardening exponent and C_{imp} is the impression strain-rate hardening coefficient.

The strain-rate hardening exponent m is a parameter that is related to the creep stress exponent n_{crp} , by the relationship

$$n_{crp} = \frac{1}{m} \quad (52)$$

Therefore, the impression creep stress exponent $n_{crp,imp}$ can be similarly obtained by substituting m with m_{imp} in equation (52).

The plots of $\ln \sigma_{imp}$ vs $\ln \dot{\epsilon}_{pl,imp}$ from the impression test simulation at various temperatures are shown from Figures 34 - 37 and the values of m_{imp} and the corresponding impression n_{crp} are tabulated in Table 16:

Temperature (°K)	m_{imp}			$n_{crp,imp}$		
	0.0250 Strain	0.0330 Strain	0.0417 Strain	0.0250 Strain	0.0330 Strain	0.0417 Strain
298	0.1692	0.1714	0.1714	5.91	5.83	5.83
323	0.1754	0.1776	0.1776	5.70	5.63	5.63
373	0.1776	0.1776	0.1798	5.63	5.63	5.56
423	0.1732	0.1754	0.1776	5.77	5.70	5.63

Table 16. m_{imp} & $n_{crp,imp}$ for Sn-Ag Solder at Various Temperatures

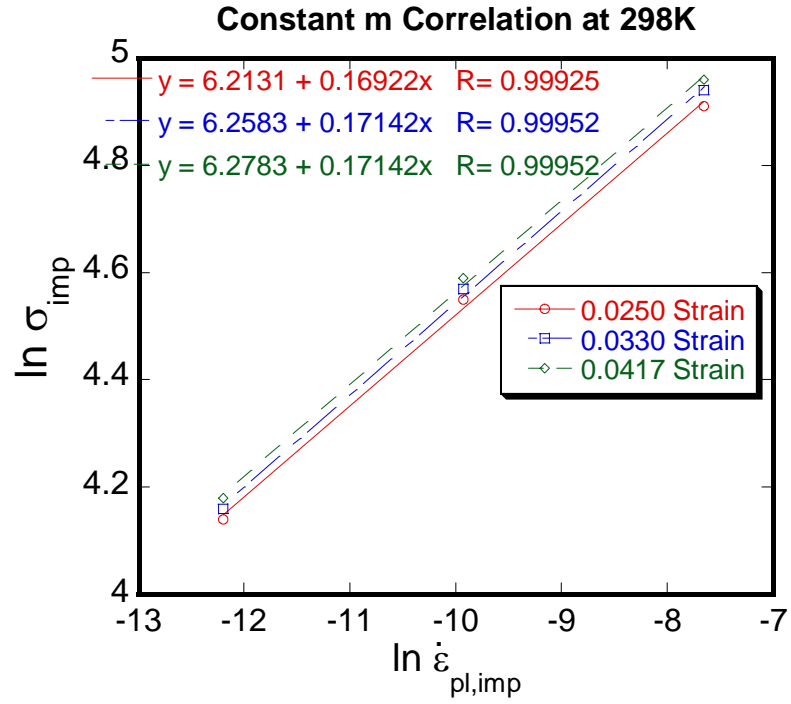


Figure 34. Plot of $\ln \sigma_{imp}$ vs $\ln \dot{\epsilon}_{pl,imp}$ for Sn-Ag Solder at 298K

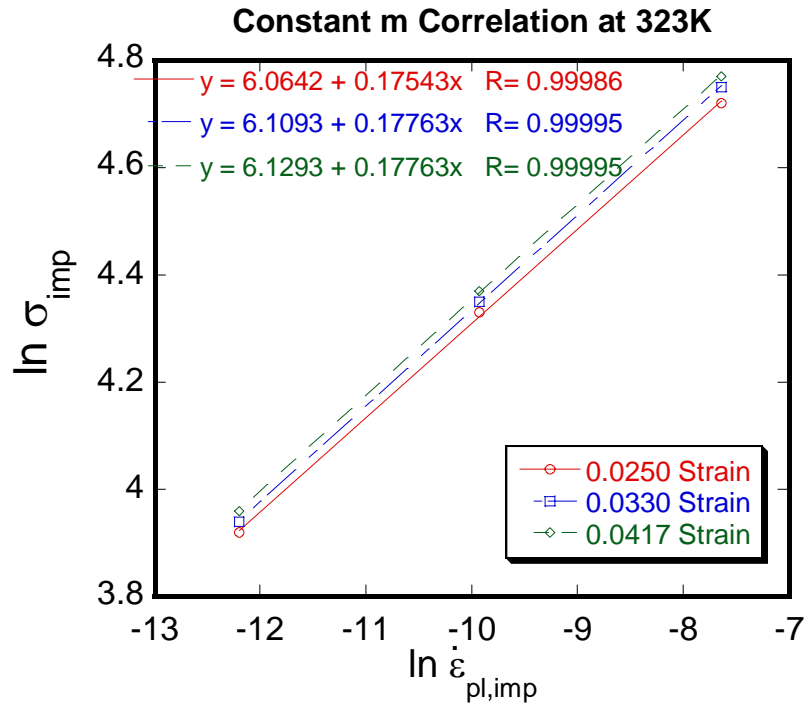


Figure 35. Plot of $\ln \sigma_{imp}$ vs $\ln \dot{\epsilon}_{pl,imp}$ for Sn-Ag Solder at 323K

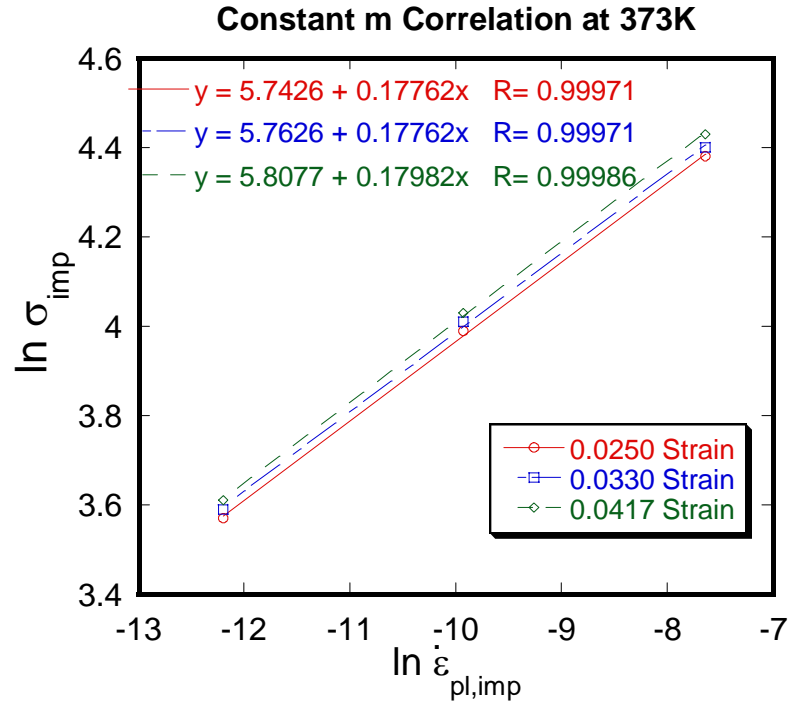


Figure 36. Plot of $\ln \sigma_{imp}$ vs $\ln \dot{\epsilon}_{pl,imp}$ for Sn-Ag Solder at 373K

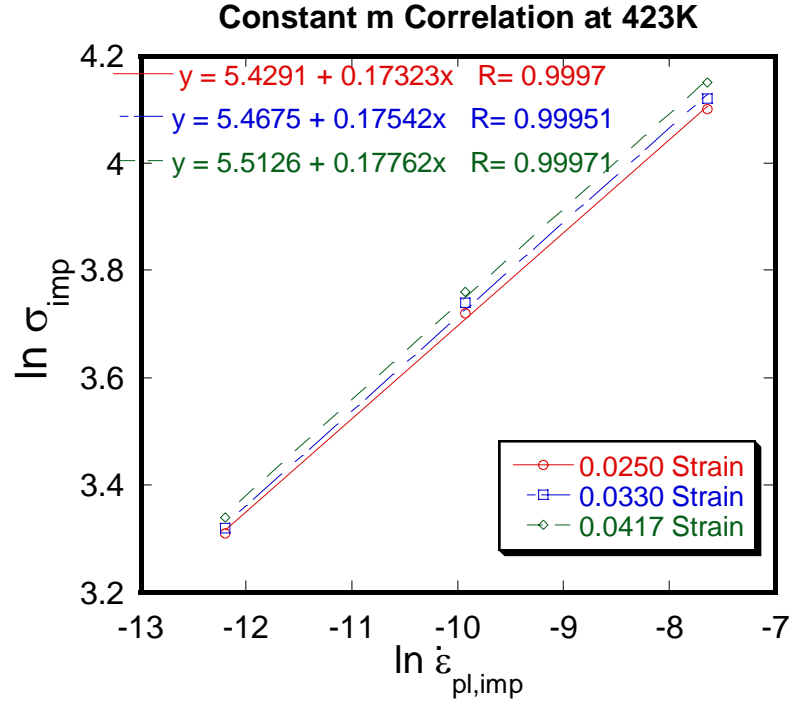


Figure 37. Plot of $\ln \sigma_{imp}$ vs $\ln \dot{\epsilon}_{pl,imp}$ for Sn-Ag Solder at 423K

C. MULTILINEAR ISOTROPIC ANALYSIS FOR ALTERNATE SOLDER

1. Impression Stress-Strain Plots for MISO Analysis

The impression stress-strain values using the MISO option for the alternate solder are tabulated below and the plots shown from Figures 38 - 41:

298K		323K		373K		423K	
Strain	Stress (MPa)	Strain	Stress (MPa)	Strain	Stress (MPa)	Strain	Stress (MPa)
0	0	0	0	0	0	0	0
1.667E-04	11.310	1.667E-04	10.262	1.667E-04	8.131	1.667E-04	5.950
3.333E-04	22.620	3.333E-04	20.524	3.333E-04	16.262	3.333E-04	11.901
5.000E-04	33.922	5.000E-04	30.771	5.000E-04	24.321	5.000E-04	17.775
6.667E-04	45.013	6.667E-04	40.738	6.667E-04	31.872	6.667E-04	23.231
8.333E-04	55.181	8.333E-04	49.706	8.333E-04	38.092	8.333E-04	27.700
1.000E-03	63.515	1.000E-03	56.907	1.000E-03	43.017	1.000E-03	31.244
1.167E-03	70.213	1.167E-03	62.766	1.167E-03	47.008	1.167E-03	34.111
1.333E-03	75.598	1.333E-03	67.446	1.333E-03	50.191	1.333E-03	36.388
1.500E-03	80.055	1.500E-03	71.329	1.500E-03	52.878	1.500E-03	38.320
1.667E-03	83.941	1.667E-03	74.703	1.667E-03	55.213	1.667E-03	39.998
2.000E-03	90.442	2.000E-03	80.362	2.000E-03	59.152	2.000E-03	42.827
2.333E-03	95.770	2.333E-03	84.980	2.333E-03	62.373	2.333E-03	45.143
2.667E-03	100.270	2.667E-03	88.875	2.667E-03	65.076	2.667E-03	47.085
3.000E-03	104.110	3.000E-03	92.200	3.000E-03	67.384	3.000E-03	48.744
3.333E-03	107.460	3.333E-03	95.088	3.333E-03	69.380	3.333E-03	50.179
3.667E-03	110.390	3.667E-03	97.611	3.667E-03	71.119	3.667E-03	51.429
4.000E-03	112.970	4.000E-03	99.830	4.000E-03	72.639	4.000E-03	52.520
4.333E-03	115.230	4.333E-03	101.770	4.333E-03	73.968	4.333E-03	53.475
4.667E-03	117.230	4.667E-03	103.490	4.667E-03	75.150	4.667E-03	54.326
5.000E-03	119.030	5.000E-03	105.030	5.000E-03	76.218	5.000E-03	55.094
6.666E-03	124.246	6.666E-03	109.142	6.666E-03	78.806	6.666E-03	56.809
8.333E-03	130.258	8.333E-03	114.416	8.333E-03	82.627	8.333E-03	59.543
9.999E-03	135.215	9.999E-03	118.779	9.999E-03	85.813	9.999E-03	61.822
1.167E-02	139.465	1.167E-02	122.528	1.167E-02	88.569	1.167E-02	63.794
1.333E-02	143.236	1.333E-02	125.861	1.333E-02	91.028	1.333E-02	65.551
1.500E-02	146.623	1.500E-02	128.857	1.500E-02	93.245	1.500E-02	67.143
1.667E-02	149.707	1.667E-02	131.585	1.667E-02	95.264	1.667E-02	68.588
1.833E-02	152.531	1.833E-02	134.086	1.833E-02	97.118	1.833E-02	69.916
2.000E-02	155.144	2.000E-02	136.399	2.000E-02	98.835	2.000E-02	71.145
2.167E-02	157.613	2.167E-02	138.586	2.167E-02	100.459	2.167E-02	72.310
2.333E-02	159.992	2.333E-02	140.693	2.333E-02	102.024	2.333E-02	73.431
2.500E-02	162.289	2.500E-02	142.729	2.500E-02	103.536	2.500E-02	74.515
2.666E-02	164.514	2.666E-02	144.699	2.666E-02	104.997	2.666E-02	75.563
2.833E-02	166.667	2.833E-02	146.605	2.833E-02	106.411	2.833E-02	76.576
3.000E-02	168.759	3.000E-02	148.458	3.000E-02	107.785	3.000E-02	77.561
3.167E-02	170.792	3.167E-02	150.258	3.167E-02	109.117	3.167E-02	78.517
3.333E-02	172.783	3.333E-02	152.020	3.333E-02	110.423	3.333E-02	79.453
3.500E-02	174.735	3.500E-02	153.746	3.500E-02	111.698	3.500E-02	80.367
3.667E-02	176.658	3.667E-02	155.447	3.667E-02	112.954	3.667E-02	81.268

Table 17. Impression Stress vs Strain Values for Alternate Solder

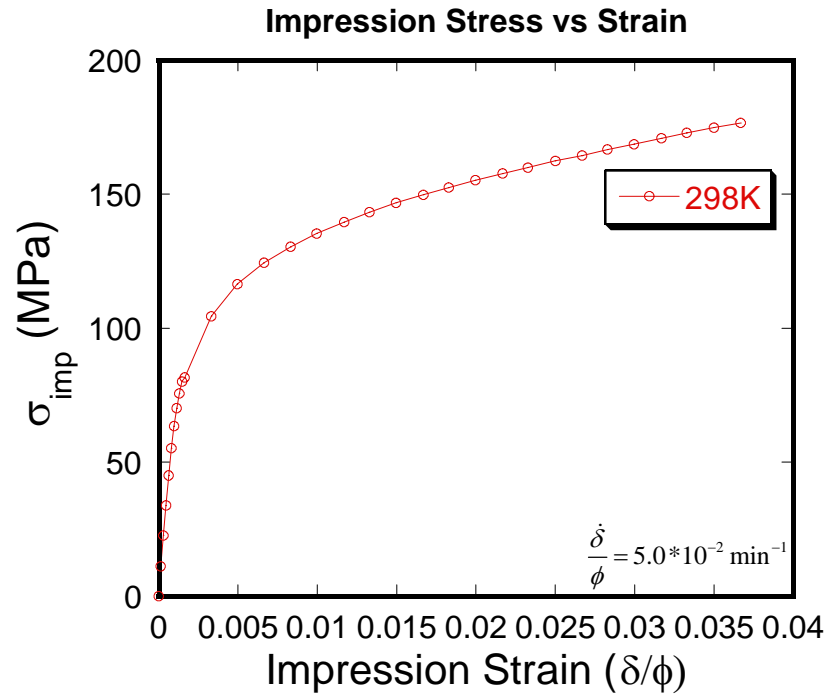


Figure 38. MISO Impression Stress-Strain Plot for Alternate Solder – 298K

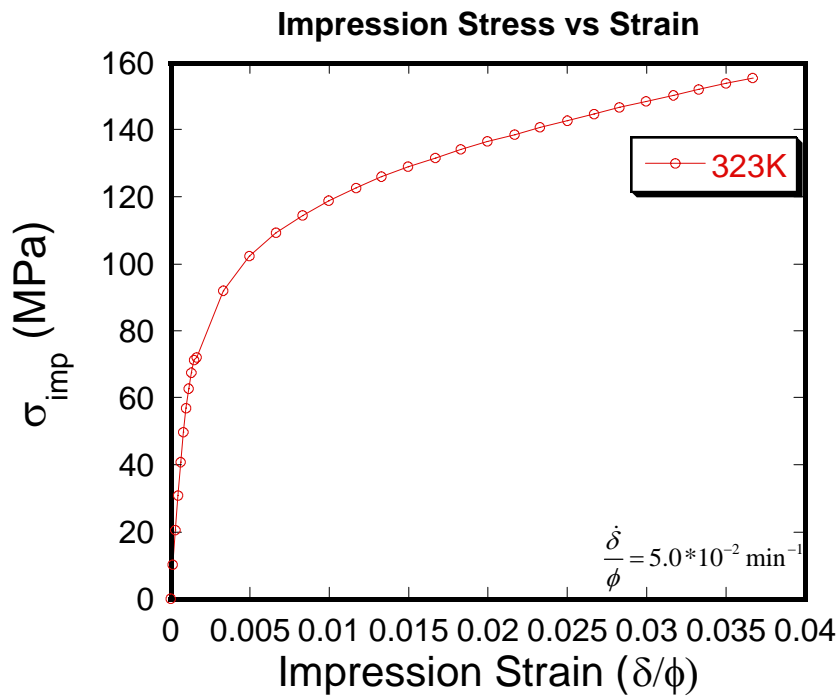


Figure 39. MISO Impression Stress-Strain Plot for Alternate Solder – 323K

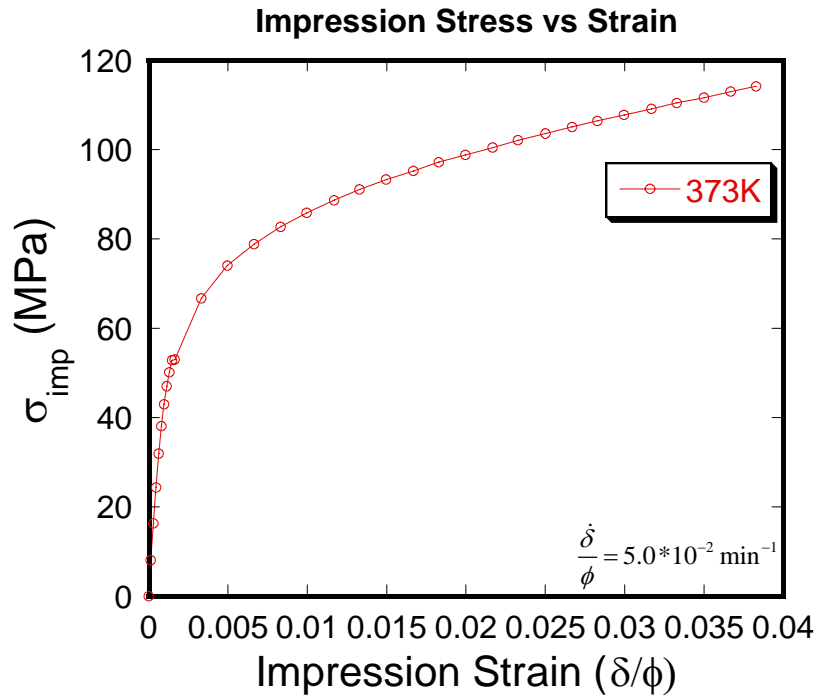


Figure 40. MISO Impression Stress-Strain Plot for Alternate Solder – 373K

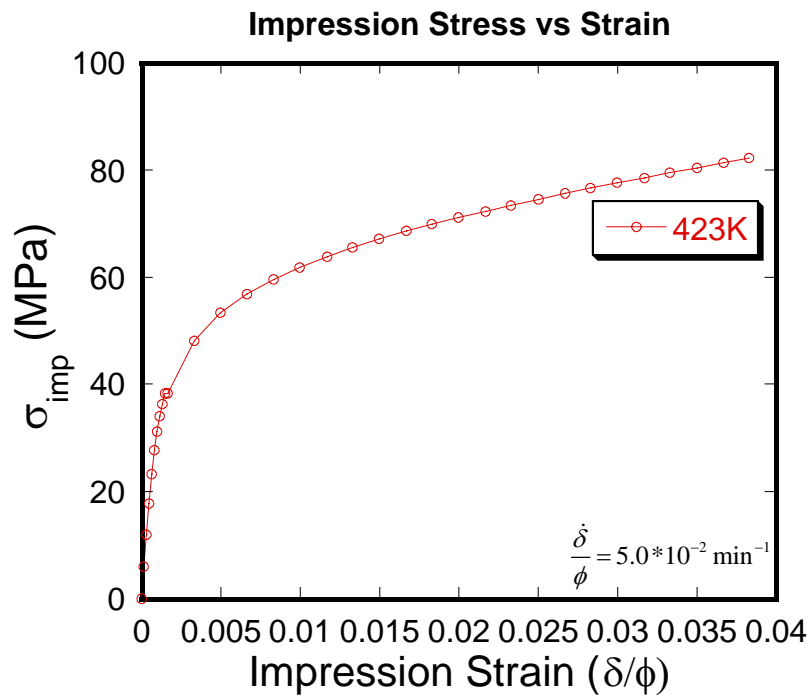


Figure 41. MISO Impression Stress-Strain Plot for Alternate Solder – 423K

2. Determination of n_{imp} and K_{imp}^{MISO} Values for MISO Analysis

Since the elastic constants used for the alternate solder is similar to that of the Sn-Ag solder, only n_{imp} and K_{imp}^{MISO} need to be determined. As before for the Sn-Ag solder, plots of $\ln (\sigma_{imp} - \sigma_{0,imp})$ vs $\ln \varepsilon_{pl,imp}$ from the impression test simulation at various temperatures were obtained and these are shown from Figures 42 - 45 with the values of n_{imp} and K_{imp}^{MISO} tabulated in Table 18:

Temperature ($^{\circ}\text{K}$)	$\ln K_{imp}^{MISO}$	K_{imp}^{MISO} (MPa)	n_{imp}
298	5.8499	347.2	0.2939
323	5.7293	307.8	0.2957
373	5.4483	232.4	0.2950
423	5.1166	166.8	0.2971

Table 18. n_{imp} & K_{imp}^{MISO} for Alternate Solder at Various Temperatures

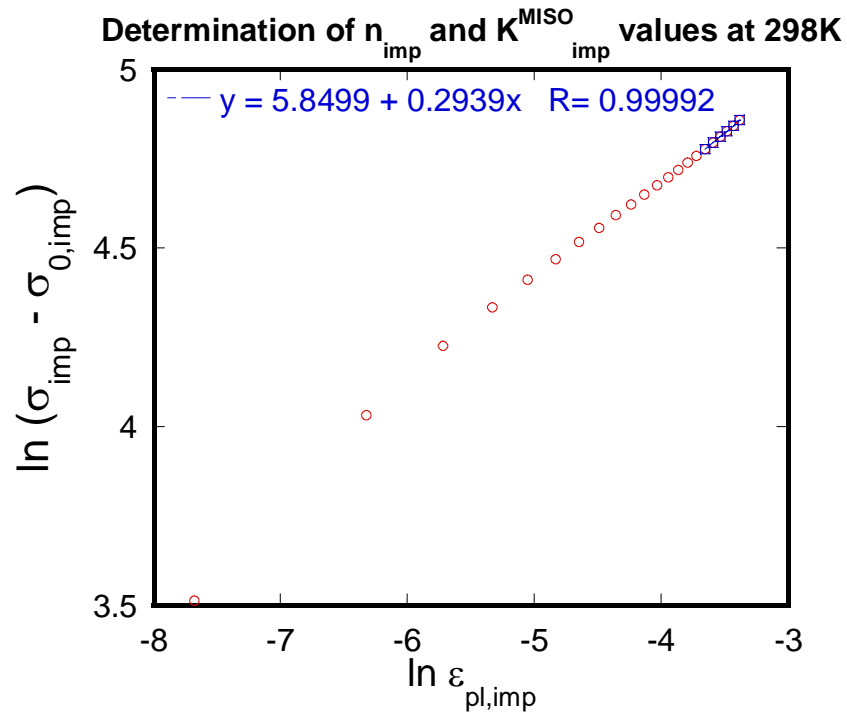


Figure 42. Plot of $\ln(\sigma_{imp} - \sigma_{0,imp})$ vs $\ln \varepsilon_{pl,imp}$ for Alternate Solder at 298K

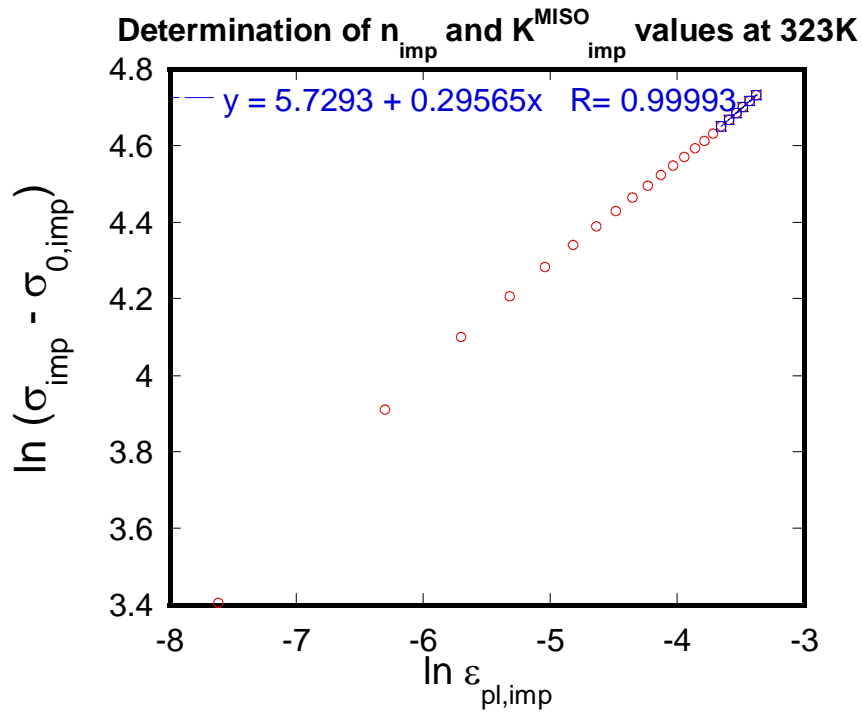


Figure 43. Plot of $\ln(\sigma_{imp} - \sigma_{0,imp})$ vs $\ln \varepsilon_{pl,imp}$ for Alternate Solder at 323K

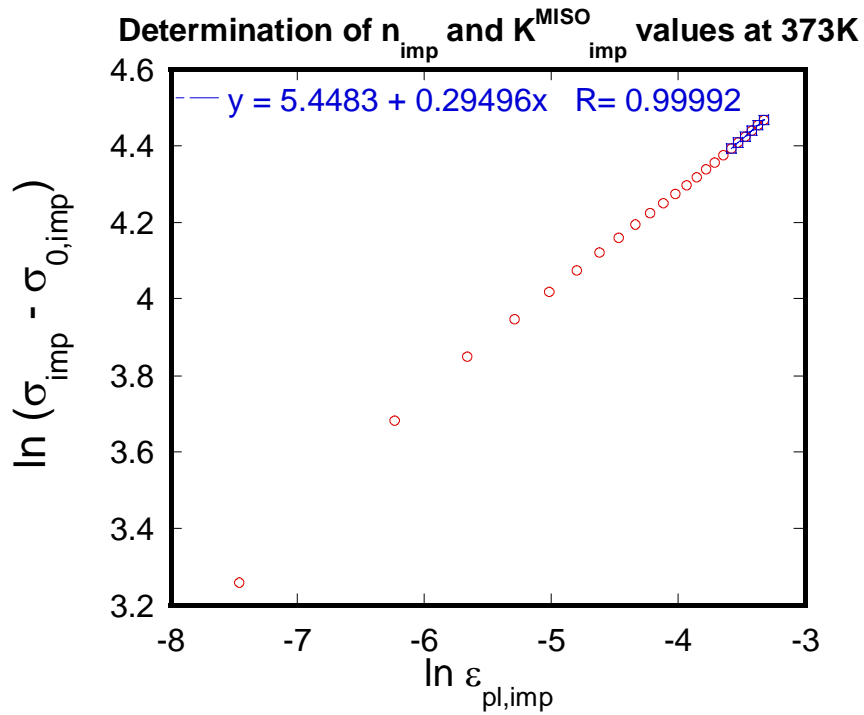


Figure 44. Plot of $\ln(\sigma_{imp} - \sigma_{0,imp})$ vs $\ln \varepsilon_{pl,imp}$ for Alternate Solder at 373K

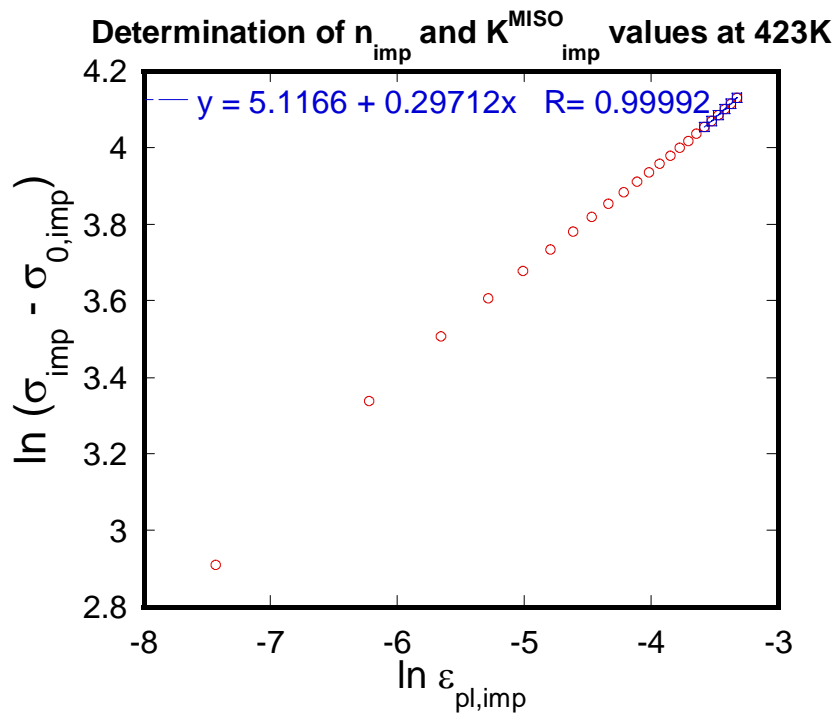


Figure 45. Plot of $\ln(\sigma_{imp} - \sigma_{0,imp})$ vs $\ln \varepsilon_{pl,imp}$ for Alternate Solder at 423K

THIS PAGE INTENTIONALLY LEFT BLANK

V. DISCUSSION

A. BILINEAR ISOTROPIC ANALYSIS FOR Sn-Ag SOLDER

1. Correlation between E_{imp}^{BISO} and E

The impression elastic modulus using the BISO option E_{imp}^{BISO} was plotted against the input uniaxial elastic modulus E in order to find out the correlation between E_{imp}^{BISO} and E . E_{imp} is related analytical to E by the expression given as

$$E_{imp} = \frac{4}{\pi(1-\nu^2)} E$$

Since the Sn-Ag solder has a Poisson's ratio of 0.35, it can be shown that

$$\frac{E_{imp}}{E} = 1.45$$

The plot of E_{imp}^{BISO} versus E is as shown:

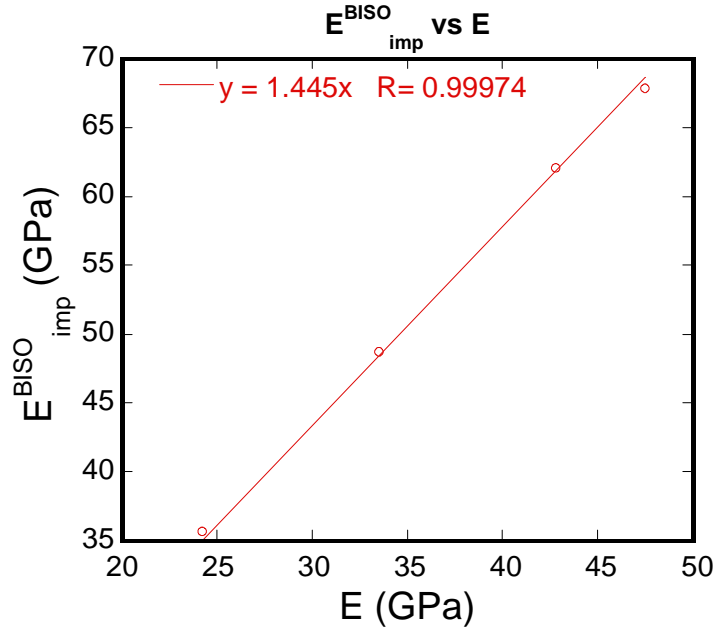


Figure 46. Plot of E_{imp}^{BISO} vs E for Sn-Ag Solder Using BISO Option

The impression elastic modulus using the BISO option E_{imp}^{BISO} was found to be approximately 1.45 times the uniaxial elastic modulus, which correlates well with the closed-form analytical value of 1.45 for this material model.

2. Correlation between K^{BISO}_{imp} and K^{BISO}

The impression strain-hardening coefficient K^{BISO}_{imp} was plotted against the input uniaxial strain-hardening coefficient for BISO analysis K^{BISO} in order to find out the correlation between K^{BISO}_{imp} and K^{BISO} . The plot of K^{BISO}_{imp} versus K^{BISO} is shown in Figure 47:

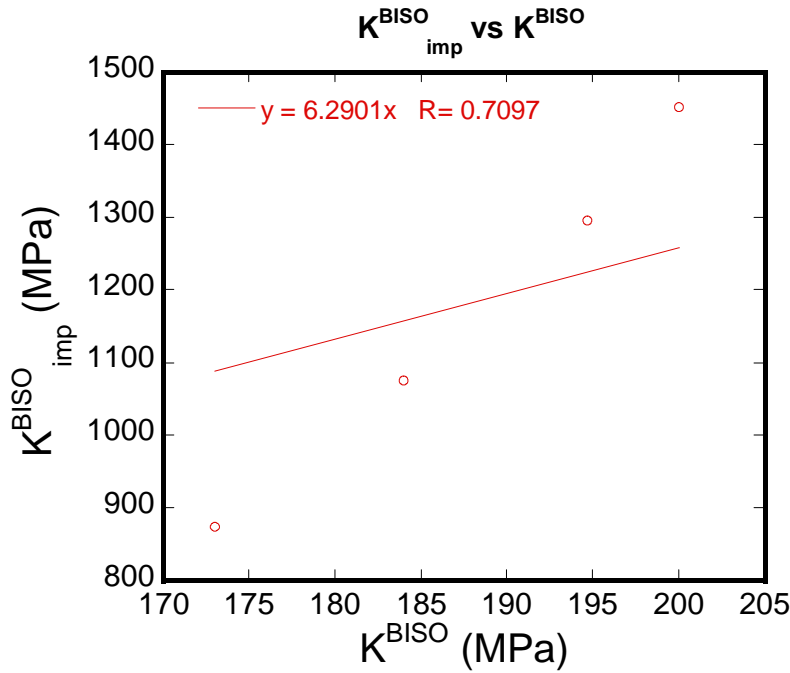


Figure 47. Plot of K^{BISO}_{imp} vs K^{BISO} for Sn-Ag Solder Using BISO Option

K^{BISO}_{imp} obtained using the BISO option was found to be approximately 6.29 times the uniaxial input K^{BISO} , but the curve fit may not be accurate since the curve-fit R-values are low. The curve fit was forced-fitted through zero-intercept; otherwise, if a linear fit were used, there would be a numerical intercept, which is erroneous since K^{BISO}_{imp} should equal zero when K^{BISO} equals zero. The errors may be due to the assumption of a strain-hardening exponent of 1.0 for the BISO option, which neglects the parabolic behavior of plastic yielding seen in most materials.

Hence, the BISO option is able to give reasonable results for the elastic analysis, but it may not be feasible in the plasticity analysis since it implicitly assumes a strain-hardening exponent of one, which may inherently give rise to errors due to the low yielding mechanical characteristics of Sn-Ag solder.

B. MULTILINEAR ISOTROPIC ANALYSIS FOR Sn-Ag SOLDER

1. Correlation between E_{imp} and E

As in the analysis using the BISO Option, since the Sn-Ag solder has a Poisson's ratio of 0.35, it can be shown that

$$\frac{E_{imp}}{E} = 1.45$$

The plot of E_{imp}^{MISO} versus E using the MISO option is as shown:

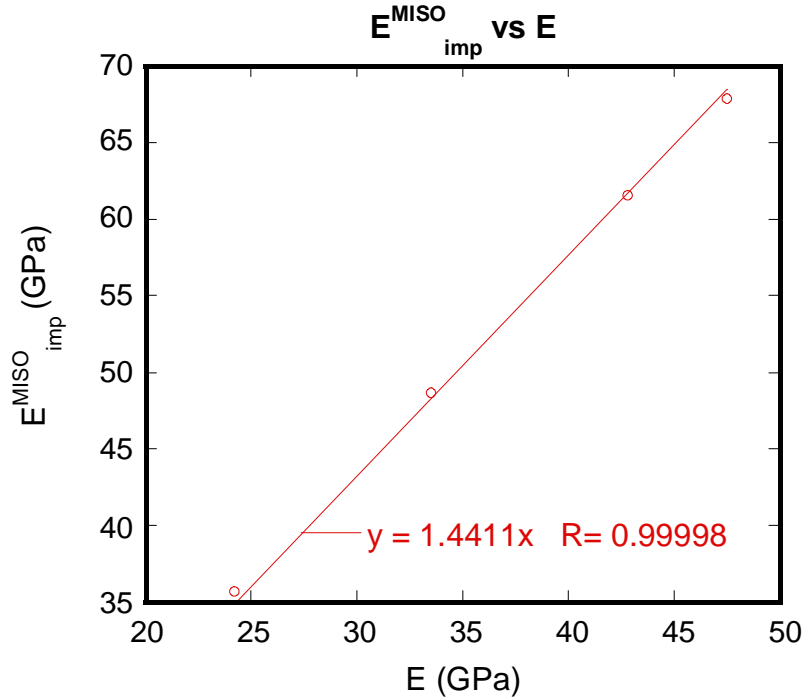


Figure 48. Plot of E_{imp}^{MISO} vs E for Sn-Ag Solder Using MISO Option

The impression elastic modulus obtained using the MISO option E_{imp}^{MISO} was found to be approximately 1.44 times the uniaxial elastic modulus E , which correlates well with the closed-form analytical value of 1.45 for this material model. Hence, the MISO option is able to give good results for the correlation of the elastic modulus.

2. Correlation between $\sigma_{YS,imp}$ and σ_{YS}

Tabor [6] stated that plastic yielding first occurs when

$$P_m = cY$$

where c is a constant of value approximately equals to three. Hence, it can be stated that the ratio of the impression yield strength, $\sigma_{YS,imp}$, and the uniaxial yield strength, σ_{YS} , may be approximately expressed as

$$\frac{\sigma_{YS,imp}}{\sigma_{YS}} \approx 3$$

The plot of $\sigma_{YS,imp}$ versus σ_{YS} at a strain offset of 0.1% and 0.2% using the MISO option is shown in Figure 49:

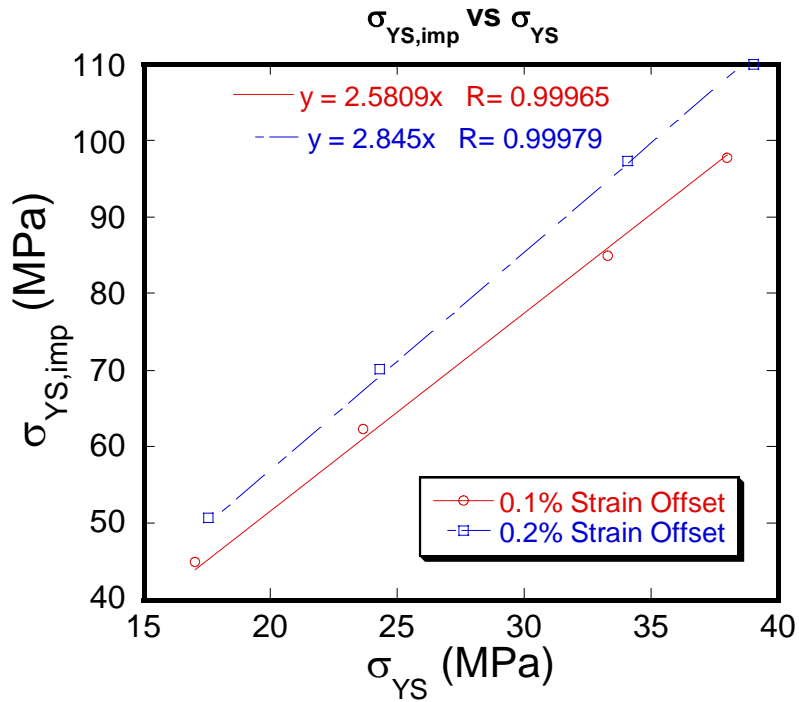


Figure 49. Plot of $\sigma_{YS,imp}$ vs σ_{YS} for Sn-Ag Solder Using MISO Option

The impression yield strength $\sigma_{YS,imp}$ obtained using the MISO option was found to be approximately 2.85 times the uniaxial yield strength σ_{YS} at a strain offset of 0.2%, and approximately 2.58 times σ_{YS} at a strain offset of 0.1%. These

values correlate well with the relationships found from literature [6]. Hence, the MISO option is able to give good results for the correlation of the yield strength.

3. Comparison of n_{imp} and n

The strain-hardening exponent n_{imp} from the impression test simulation should be invariant across test conditions since the input strain-hardening exponent n is 0.17 for all the simulated conditions for the Sn-Ag solder.

The chart of n_{imp} and n is plotted and compared as shown in Figure 50:

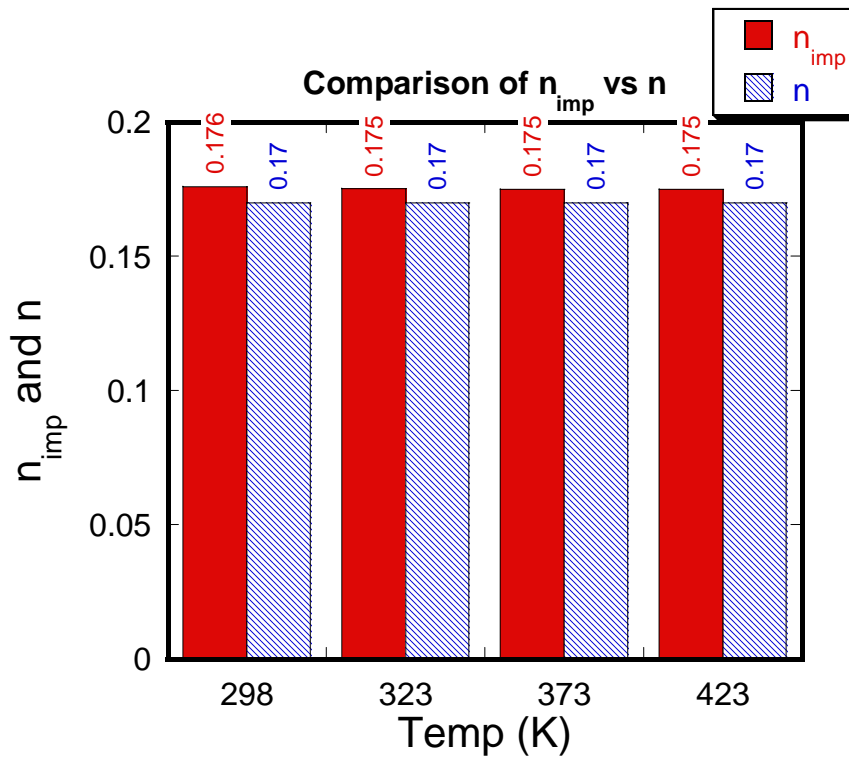


Figure 50. Chart of n_{imp} and n across Various Temperatures for Sn-Ag Solder

It can be seen from the chart that n_{imp} is relatively invariant across temperatures and correlates well with the input uniaxial strain-hardening exponent of 0.17. Hence, impression testing may be used to directly obtain the impression strain-hardening exponent n_{imp} , which is approximately equivalent to the uniaxial input strain-hardening exponent n . Therefore, it can be determined that n_{imp}/n has a factor of approximately one.

4. Correlation between K_{imp}^{MISO} and K^{MISO} for Sn-Ag Solder

The impression strain-hardening coefficient K_{imp}^{MISO} was plotted against the input uniaxial strain-hardening coefficient K^{MISO} in order to find out the correlation between K_{imp}^{MISO} and K^{MISO} .

The plot of K_{imp} versus K is shown in Figure 51:

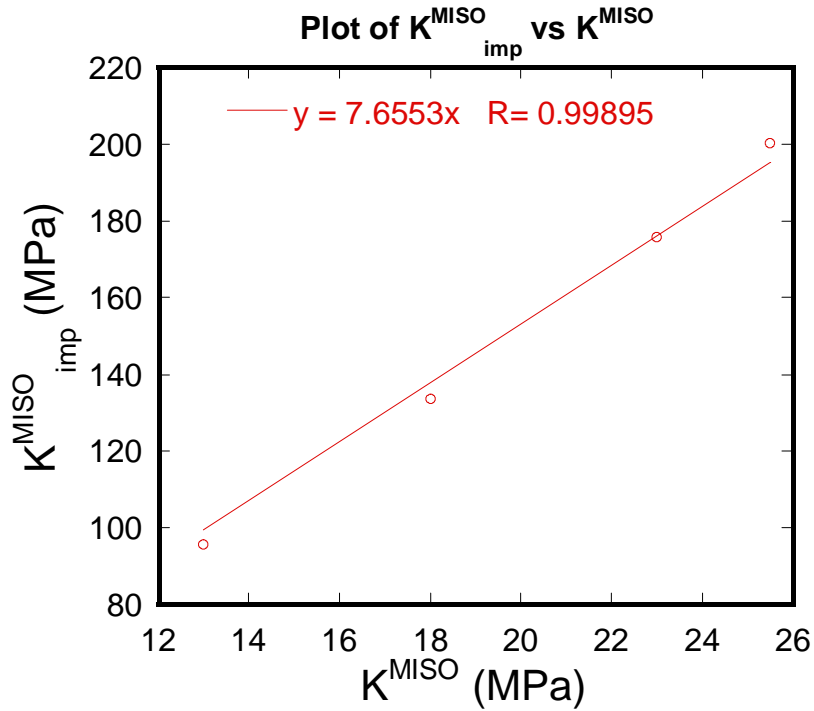


Figure 51. Plot of K_{imp}^{MISO} vs K^{MISO} for Sn-Ag Solder

K_{imp}^{MISO} obtained from the impression test simulation is approximately 7.66 times the value of K^{MISO} obtained from uniaxial testing for this Sn-Ag solder. This means that impression testing may be used to obtain the impression strain-hardening coefficient K_{imp}^{MISO} , and the uniaxial strain-hardening coefficient K^{MISO} of the material may be obtained by dividing K_{imp}^{MISO} by a factor of 7.66.

However, the above factor is only based on one set of n and K values, and hence an alternate solder with a different n and K value would be used to determine the sensitivity of the factor, which will be addressed later.

5. Comparison of m_{imp} and $n_{crp,imp}$ with m and n_{crp}

From Figure 52, it can be seen that the values of the impression strain-rate hardening exponent m_{imp} are relatively close to the uniaxial strain-rate hardening exponent m input of 0.1818. That implies that the impression creep stress exponent $n_{crp,imp}$ is comparatively equivalent to the uniaxial input creep stress exponent n_{crp} value of 5.5 as shown in Figure 53, since $n_{crp,imp}$ is the reciprocal of m_{imp} as shown in Equation (52). In addition, it can be seen that n_{crp} gives a better correlation at larger strain values and this is evident across all the temperatures tested.

The largest deviation of $n_{crp,imp}$ with n_{crp} is about 7.5%, which occurs over the test condition of 298K at a strain of 0.0250, while the smallest deviation of $n_{crp,imp}$ with n_{crp} is about 1.1%, which occurs over the test condition of 373K at a strain of 0.0417.

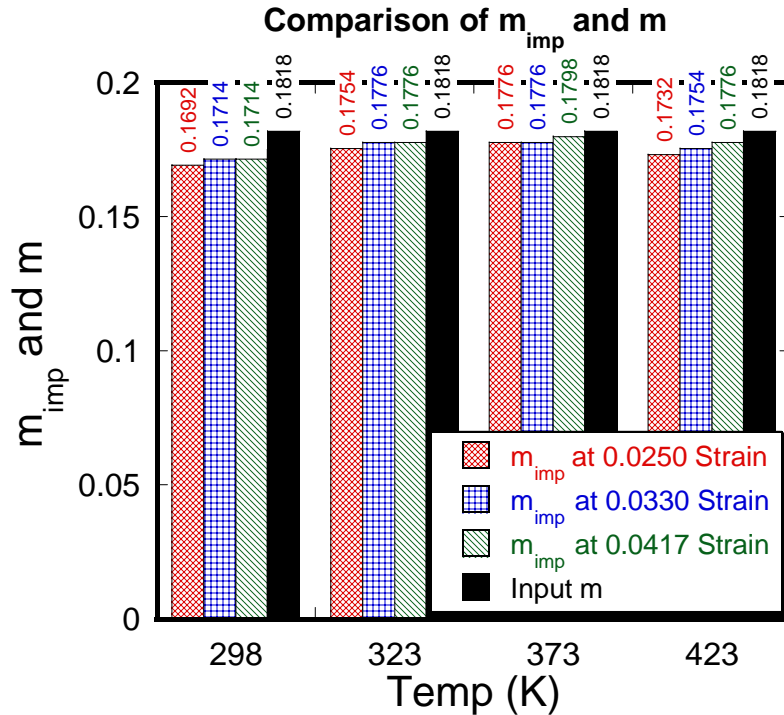


Figure 52. Chart of m_{imp} and m at Various Strains and Temperatures for Sn-Ag Solder

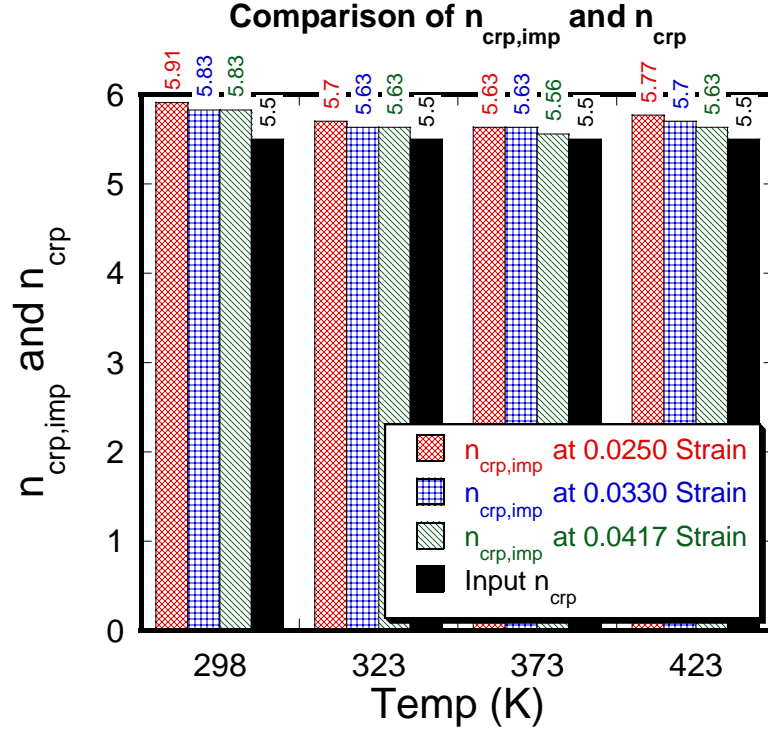


Figure 53. Chart of $n_{crp,imp}$ and n_{crp} at Various Strains and Temperatures for Sn-Ag Solder

$n_{crp,imp}$ is obtained from the reciprocal of m_{imp} , and m is the reciprocal of n_{crp} . Hence, it can be shown that impression testing is a quick and effective method to get the impression strain-rate hardening exponent m_{imp} , as well as the impression creep stress exponent $n_{crp,imp}$, which in this study shows that it is approximately equivalent to the uniaxial creep stress exponent n_{crp} .

C. MULTILINEAR ISOTROPIC ANALYSIS FOR ALTERNATE SOLDER

1. Comparison of n_{imp} and n

As before for the Sn-Ag solder, the strain hardening exponent from the impression test simulation for the alternate solder should be invariant across test conditions and should be relatively similar to the uniaxial input strain hardening exponent at a given strain condition. The correlations of the elastic constants for the alternate solder are similar to that of the Sn-Ag solder.

The chart of n_{imp} and n is plotted and compared as shown in Figure 54:

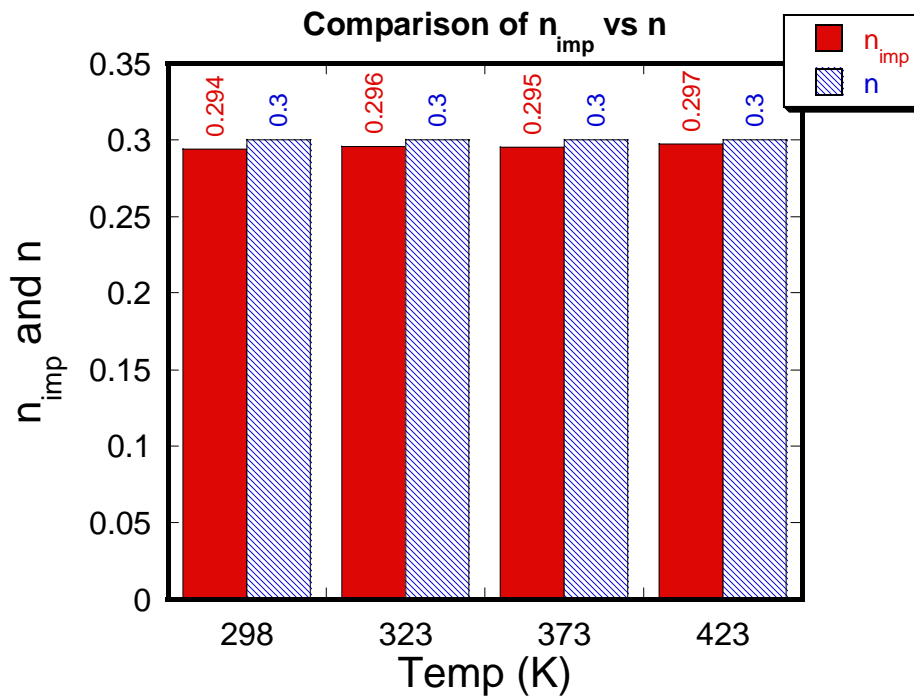


Figure 54. Chart of n_{imp} and n across Various Temperatures for Alternate Solder

It can be seen from the chart that n_{imp} is relatively invariant across temperatures and correlates well with the input uniaxial strain-hardening exponent of 0.30. Hence, impression testing may be used to directly obtain the impression strain-hardening exponent n_{imp} , which is approximately equivalent to the uniaxial input strain-hardening exponent n . Therefore, it can be determined that n_{imp}/n has a factor of approximately one

2. Correlation between K^{MISO}_{imp} and K^{MISO} for Alternate Solder

Similarly as for the Sn-Ag solder, the impression strain-hardening coefficient K^{MISO}_{imp} was plotted against the input uniaxial strain-hardening coefficient K^{MISO} in order to find out the correlation between K^{MISO}_{imp} and K^{MISO} .

The plot of K^{MISO}_{imp} versus K^{MISO} is shown in Figure 55:

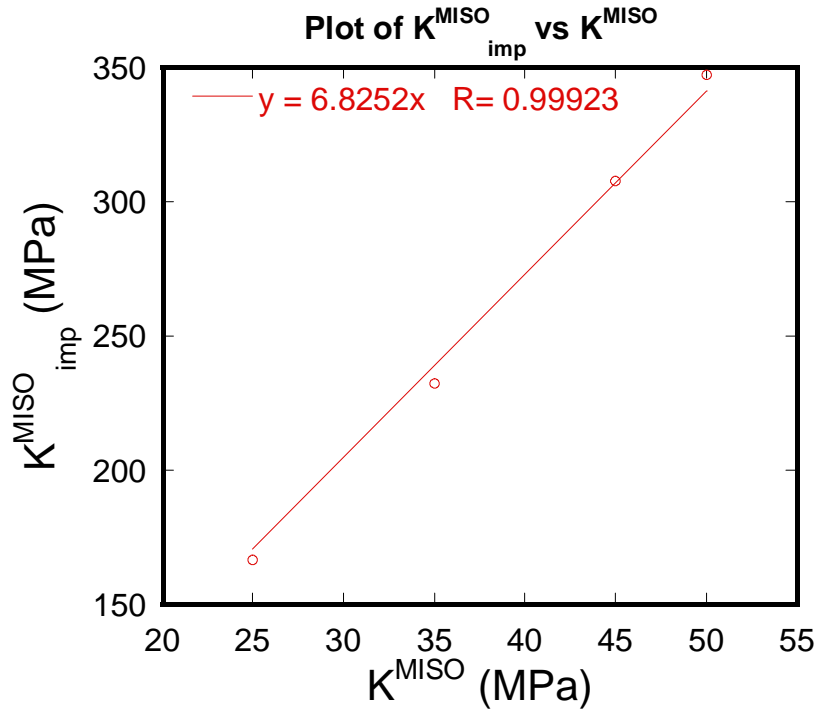


Figure 55. Plot of K^{MISO}_{imp} vs K^{MISO} for Alternate Solder

K^{MISO}_{imp} obtained from the impression test simulation is approximately 6.83 times the value of uniaxial input K^{MISO} for this alternate solder. Although there is a difference in the value of K^{MISO}_{imp} vs K^{MISO} using different n and K^{MISO} uniaxial input values, the difference is only approximately 10%.

However, in order to get a better estimate of the correlation between K^{MISO}_{imp} and K^{MISO} , all the data points from both the Sn-Ag solder and the alternate solder are curve-fitted and the plot is shown in Figure 56:

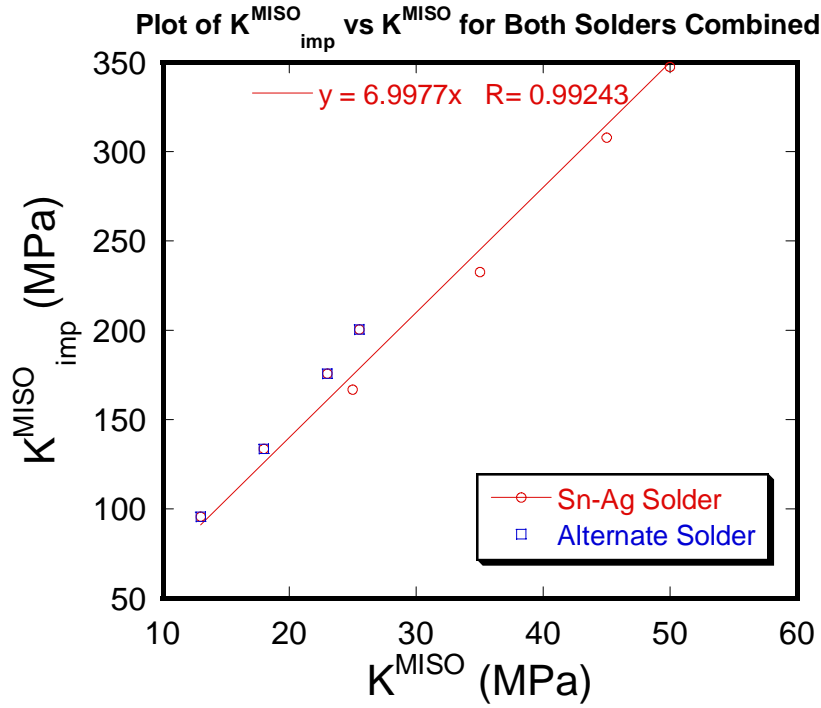


Figure 56. Plot of K^{MISO}_{imp} vs K^{MISO} for Sn-Ag Solder and Alternate Solder Combined

It can be seen that K^{MISO}_{imp} vs K^{MISO} for the curve fit of all the data points yields a correlation factor of about 7.0. This means that impression testing may be used to obtain the impression strain-hardening coefficient K^{MISO}_{imp} , and the uniaxial strain-hardening coefficient K of the material may be obtained by dividing K^{MISO}_{imp} by this correlation factor of 7.0.

Hence, K^{MISO}_{imp}/K^{MISO} gives an approximate factor of 7.0 for the simulated strain conditions and it is relatively independent of test conditions and material properties.

D. RECOMMENDATION FOR FUTURE WORK

The simulation work performed in this study covers impression testing using flat-tip indenters on Sn-Ag solder. Future work that can be performed includes the following:

- The simulation study could be expanded to include other solder materials having different n and K values
- Experimental work could be performed to correlate the simulation results with actual test results
- Other constitutive stress-strain relations to describe the onset of plastic yielding could be used in comparison to the Holloman equation
- Other indenter geometries may be used to determine their effects on stress-strain relations in impression testing
- The boundary conditions and test conditions could be expanded to obtain more data points for correlation analysis

VI. CONCLUSION

The simulation work performed in this study shows that impression testing is a useful method to obtain mechanical properties of small materials like the Sn-Ag solder. Hence, elastic, plastic and creep properties of materials can be obtained from the impression stress-strain curves by correlating them with uniaxial test results.

A summary of the correlation factors between impression testing and uniaxial test results is shown in Table 19:

Description	Impression Test Parameter	Uniaxial Input Parameter	Correlation Factor
Elastic Modulus	E_{imp}^{BISO}	E	$E_{imp}^{BISO}/E \sim 1.45$
	E_{imp}^{MISO}	E	$E_{imp}^{MISO}/E \sim 1.44$
Yield Strength	$\sigma_{YS,imp}$	σ_{YS}	$\sigma_{YS,imp}/\sigma_{YS}$ at 0.1% strain offset ~ 2.58
			$\sigma_{YS,imp}/\sigma_{YS}$ at 0.2% strain offset ~ 2.85
Strain-hardening Exponent	n_{imp} for Sn-Ag Solder	n for Sn-Ag Solder	$n_{imp}/n \sim 1.0$ for Sn-Ag Solder
	n_{imp} for Alternate Solder	n for Alternate Solder	$n_{imp}/n \sim 1.0$ for Alternate Solder
Strain-hardening Coefficient	K_{imp}^{BISO} for Sn-Ag Solder	K^{BISO} for Sn-Ag Solder	$K_{imp}^{BISO}/K^{BISO} \sim 6.29$
	K_{imp}^{MISO} for Sn-Ag Solder	K^{MISO} for Sn-Ag Solder	$K_{imp}^{MISO}/K^{MISO} \sim 7.66$ for Sn-Ag Solder
	K_{imp}^{MISO} for Alternate Solder	K^{MISO} for Alternate Solder	$K_{imp}^{MISO}/K^{MISO} \sim 6.83$ for Alternate Solder
	K_{imp}^{MISO} for both Solders	K^{MISO} for both Solders	$K_{imp}^{MISO}/K^{MISO} \sim 7.0$ for both Solders
Strain-rate Hardening Exponent	m_{imp}	m	$m_{imp}/m \sim 1.0$
Creep Stress Exponent	$n_{crp,imp}$	n_{crp}	$n_{crp,imp}/n_{crp} \sim 1.0$

Table 19. Summary of Correlation Factors

It can be seen that the analytical solution relating E_{imp} and E holds since the BISO option gives an E^{BISO}_{imp}/E ratio of 1.45 and the MISO option gives an E^{MISO}_{imp}/E ratio of 1.44, which compares well to the analytical solution of 1.45 for this material model. In addition, the simulation gives an $\sigma_{YS,imp}/\sigma_{YS}$ ratio of 2.85 at a strain offset of 0.2% and an $\sigma_{YS,imp}/\sigma_{YS}$ ratio of 2.58 at a strain offset of 0.1%, which coincides well with the widely accepted experimental values of three from Tabor's [6] tabulation.

The simulation also shows that impression testing can be used to obtain the impression strain hardening exponent n_{imp} , which is invariant across temperatures and is approximately equivalent to the uniaxial input strain hardening exponent n . The value of K^{MISO}_{imp}/K^{MISO} was found to be approximately 7.0 from the simulation, which implies that the material K value can be obtained from impression testing by dividing K^{MISO}_{imp} by a factor of 7.0. The correlation for the strain-hardening coefficient using the BISO option is poor since the curve-fit R-values are low. The errors may be due to the assumption of a strain-hardening exponent of 1.0 for the BISO option, which neglects the parabolic behavior of the plastic yielding seen in most materials.

Impression testing can also be used to obtain the creep stress exponent n_{crp} , which is the reciprocal of the strain-rate hardening exponent m . Hence, m_{imp} can be easily obtained from impression testing and its reciprocal is the impression creep stress exponent $n_{crp,imp}$, which is approximately equivalent to n_{crp} from the uniaxial input.

Therefore, impression testing is the method of choice for testing small-sized materials such as lead-free solders since the parameters obtained from impression testing can be easily correlated to uniaxial test results of which mechanical properties of materials can be easily extracted.

LIST OF REFERENCES

- [1] W.D. Callister, *Materials Science and Engineering: An Introduction*, 6th Ed., J.Wiley & Sons, New York, (2003)
- [2] J.W. Harding and I.N. Sneddon, Proc. Cambridge Phil. Soc. 41, 16 (1945)
- [3] I.N. Sneddon, Int. J. Eng. Sci. 3, 47 (1965)
- [4] K.L. Johnson, *Contact Mechanics*, Cambridge University Press, Cambridge, 1985
- [5] R. Hill, *The Mathematical Theory of Plasticity*, Clarendon Press, Oxford, 1998
- [6] D. Tabor, *The Hardness of Metals*, Oxford University Press, London, (1951)
- [7] N.A. Stillwell and D. Tabor, Proc. Phys. Soc. 78, 169 (1961)
- [8] D. Tabor, Proc. R. Soc. A192, 247 (1948)
- [9] W.C. Oliver and G.M. Pharr, J. Mater. Res. 7, 1564 (1992)
- [10] S.N.G. Chu and J.C.M. Li, J. Mater. Sci. 12, 2200 (1977)
- [11] G.M. Pharr, Mater. Sci. Eng. A253, 151 (1998)
- [12] J.A. Knapp, D.M. Follstaedt, S.M. Myers, J.C. Barbour, and T.A. Friedman, J. Appl. Phys. 85, 1460 (1999)
- [13] R. Saha and W.D. Nix, Acta Mater. 50, 23 (2002)
- [14] A.C. Fischer-Cripps, J. Mat. Res. 16, 3050 (2001)
- [15] A.K. Bhattacharya and W.D. Nix, Intl. J. Solids Structures 24, 881 (1988)
- [16] G.M. Pharr, W.C. Oliver, and F.R. Brotzen, J. Mater. Res. 7, 613 (1992)
- [17] R.B. King, Int. J. Solids Structures 3, 1657 (1987)
- [18] M.F. Doerner and W.D. Nix, J. Mater. Res. 1, 601 (1986)
- [19] A. Bolshakov, G.M. Pharr, J. Mater. Res. 13, 1049 (1998)

- [20] J.C. Hay, A. Bolshakov, and G.M. Pharr, J. Mater. Res. 14, 2296 (1999)
- [21] J.L. Hay and P.J. Wolff, J. Mater. Res. 16, 1280 (2001)
- [22] M. Dao, N. Chollacoop, K.J. Van Vliet, T.A. Venkatesh, and S. Suresh, Acta Mater. 49, 3899 (2001)
- [23] Y.T. Cheng and C.M. Cheng, J. Mater. Res. 14, 3493 (1999)
- [24] A.E. Giannakopoulos and S. Suresh, Scripta Mater. 40, 1191 (1999)
- [25] J.S. Field and M.V. Swain, J. Mater. Res. 8, 297 (1993)
- [26] J. Alcala, A.C. Barone, and M. Anglada, Acta Mater. 48, 3451 (2000)
- [27] H.Y. Yu and J.C.M. Li, J. Mater. Sci. 12, 2214 (1977)
- [28] F. Yang and J.C.M. Li, Mater. Sci. Eng., A201, 40 (1995)
- [29] F. Yang, J.C.M. Li, and C.W. Shih, Mater. Sci. Eng., A201, 50 (1995)
- [30] F. Yang, J. Chen, I. Seidmann, and J.C.M. Li, Mater. Sci. Eng., A207, 30 (1996)
- [31] F. Yang, Int. J. Mech. Sci. Vol. 40 No. 1, 87 (1998)
- [32] K. Balani and F. Yang, Phys. Stat. Sol. (a) 198, No. 2, 387 (2003)
- [33] S.D. Rani and G.S. Murthy, Mater. Sci. and Tech. Vol. 20, 7, 885 (2004)
- [34] D. Pan, R.A. Marks, I. Dutta, R. Mahajan, and S.G. Jadhav, Rev. Sci. Instrum., Vol. 75, No. 12, 5244 (2004)
- [35] D. Pan and I. Dutta, Mater. Sci. Eng, A379, 154 (2004)
- [36] H.Y. Yu, M.A. Imam., and B.B. Rath, J. Mater Sci 20, 636 (1985)
- [37] R.W. Hertzberg, *Deformation and Fracture Mechanics of Engineering Materials*, J. Wiley & Sons, New York, (2003)

INITIAL DISTRIBUTION LIST

1. Defense Technical Information Center
Ft. Belvoir, Virginia
2. Dudley Knox Library
Naval Postgraduate School
Monterey, California
3. Mechanical Engineering Curricular Office
Naval Postgraduate School
Monterey, California
4. Department Chairman, Mechanical Engineering
Naval Postgraduate School
Monterey, California
5. Professor Indranath Dutta
Department of Mechanical Engineering, Naval Postgraduate School
Monterey, California
6. Professor Yeo Tat Soon
Director, Temasek Defence Systems Institute
National University of Singapore
Singapore
7. Ms Tan Lai Poh
Senior Admin Officer, Temasek Defence Systems Institute
National University of Singapore
Singapore
8. Mr How, Yew Seng
Singapore Technologies Engineering
Singapore